Development of KUbeSat-1 Payloads PCRD and HiCalK

Brendon Cory Madison

B.Sc. Pre-Professional Physics, University of Kansas, 2017

Submitted to the graduate degree program in Department of Physics and Astronomy and the Graduate Faculty of the University of Kansas in partial fulfillment of the requirements for the degree of Master of Physics.

David Z. Besson, Chairperson

Committee members

Graham W. Wilson

John P. Ralston

Date defended: December 1, 2020

The Dissertation Committee for Brendon Cory Madison certifies
that this is the approved version of the following dissertation :

Development of KUbeSat-1 Payloads PCRD and HiCalK

David Z. Besson, Chairperson

Date approved: null

Abstract

KUbeSat-1 is set to be the first CubeSat mission from Kansas; flown by students from the Physics and Astronomy and Aerospace Engineering departments. It has two physics payloads, Primary Cosmic Ray Detector (PCRD) and High-Altitude Calibration KUbeSat (HiCalK). This thesis work is on the physics of the KUbeSat-1 mission and its payloads. For PCRD an original detector design and data acquisition system have been in development. PCRD detector geometry is made to measure horizontally propagating particles in low earth orbit with an energy threshold of a few MeV of energy. A new parameter, radiation gain, is proposed as a method of quantifying Cherenkov and scintillation radiation in scintillators in order to differentiate particle species, and their energies, in small volume detectors. This method will make PCRD the first CubeSat payload to use pulse shape discrimination. Summarily, the PCRD payload aims to be a proof of concept for future high energy physics experiments done on CubeSats. A new antenna design, dubbed 'Bivaldi', is made for HiCalK. It features low pulse dispersion, 200-2000 MHz wide-band RF performance and 25-degree beam width, all within an 8x8x8 cm^3 satellite space. A piezoelectric pulser architecture is chosen for driving the antenna. In testing it is found that piezoelectricity can generate RF pulses in vacuum. A new piezoelectric model, employing ferroelectric dipole oscillations and dissipation via rotational Brownian motion is proposed to explain these observations. The stress response of a piezoelectric is tested in a simple, undergraduate accessible, experiment and recovers the standard piezoelectric linear relationship with voltage and stress.

Acknowledgements

This is by no means a complete list as the human mind is in a constant state of flux; our memories, like patterns on the ocean, come and go regardless of our wishes. The illusion of reality is like all magic tricks; by choosing to believe in the magic we surrender. Choosing to be critical shows how paper thin everything is. Being a scientist gives us the sight to write upon the paper, but it is always in silence. The universe is the eternally distant pen pal, never returning letters and only offering a solemn gaze from afar. For this I thank the universe, and all its beings, for allowing me this relationship.

From my high school years, wrought with stress and depression, I have a handful of people that kept me afloat. Drew Keiter, my physics teacher, showed me how interesting, and especially funny, physics can be. Eric Skoglund who taught me advanced mathematics and, tolerated my poor performance in it, as it kept me motivated to come to school. Anna Koehne who, despite my adolescent cringe, would fill me with positivity and believed in me. Dr. David Sinha for teaching me the value of being confident in my knowledge and skills. Mike McRoberts who taught me the value of nature and the value of human connections. I am especially grateful to my then therapist Brooke Wesley for being my mental interlocutor and giving me meaningful tools for adapting to a world that clearly, is not meant for autistic or depressed people. With the greatest of praise, I thank my friend Anthem Shipton who is simultaneously deserving of more and less than he has ever been given. We bonded over many things that I now realize could only happen because we both were broken individuals that lived in a part of the world that did not tolerate broken individuals.

From my undergraduate tenure at the University of Kansas I met my future advisor Dave Besson, who I am forever grateful to and indebted to. I know I am poor at showing my gratitude, but I truly value your input and mentorship. You have kept me, and some of my research, grounded in reality and, without you, I don't think I could have gotten into graduate physics.

I also engaged in our Society of Physics Students chapter where I worked alongside Nesar Ramachandra, Billie Lubis, Pierce Giffin, without who I would not have been able to grow from being a casual physicist to ravenously seeking out professional physics.

I am thankful for Dr. Cristoph Royon who I did research for and, under whom, I was mentored by Dr. Hussein Al-Ghoul who taught me most of the basics of experimental particle physics.

Under the Fermilab outreach program of QuarkNet I was able to work as a mentor with our chapter's leader Jim Deane who showed me how valuable outreach programs can be for youth pursuing science. I personally mentored one of these youths, Brady Volkmann, who I am thankful for. Brady displayed a great affinity for work and knowledge that I hope I can emulate and also inspire into students.

I am thankful to the University of Kansas Department of Physics and Astronomy for allowing me to be a graduate student of your department after I spent two years working to improve my graduate school application.

Into my graduate physics career, I've come to value my relationship with Dr. Graham Wilson, whose drive of curiosity has inspired me. I am thankful for Dr. John Ralston who has shown me the value of critical thinking and communication of these thoughts to our world. I am thankful for Dr. Greg Rudnick for being a graduate chairman who clearly values the lives of his students and is always willing to take time to help said students.

I am thankful to Dr. Judy Wu for her kindness when I TA'd for her. She also taught me the value of balancing work and life.

I am thankful to Dr. Ben Sikes who has shown me the value of interdisciplinary science and has been a source of incredible discussion and motivation towards new ideas.

Through my work on the KUbeSat-1 mission I have become indebted to and thankful for many people. To Dr. Mark Ewing and Dr. Brian Kaplinger I am grateful for working as the heads and faculty sponsors of the KUbeSat-1 mission. To Dr. Brian Kaplinger I am particularly inspired by as he has shown me it is possible to be successful in academia even when you are born into hardship. I am thankful for Madison Sargent for leading the student side of KUbeSat-1 during

its incarnation and Arno Prinsloo for leading it since. I am thankful for the work of the other Aerospace leads particularly Taylor George, Lee Taylor, Bailey Miller, Shravan Kaundinya. I am thankful for the work done by student workers Pedro Martinez Lopez and Ankur Patil. I have valued my correspondence with both Dr. Jerry Manweiler and Dr. Doug Patterson, without which I would have less of an understanding of space and satellite capable detectors than I currently do.

As a member of the Particle Astrophysics group I have come to work with many gifted individuals. Again, I thank Dr. Dave Besson for allowing me to be a part of this group and organizing this group. I have valuable mentoring from Dr. Alexander 'Sasha' Novikov, Dr. Steven Prohira, and most of all Dr. Uzair Latif who inspired me to go beyond what I would normally consider sufficient performance. Though I likely will never match him. I am thankful to my peers Andrew Shultz, Alisa Nozdrina, Mitch Magnuson, Mohammad Seikh for our discussions and cooperation.

As an extension of our group I've worked with many undergraduate students who I've come to value and are thankful for. I am thankful for Hadrian Salento, whose studiousness is matched by ingenuity in a way that seems too clear to come from a person so young. I am thankful for Cristina Parra who entertained my, potentially misplaced, ideas of merging physics and biology. I am thankful for Colin Sherman for his work towards a solution on the aforementioned union of biology and physics.

I am thankful for Mark Stockham and Allen Hase for turning dreams and ideas into reality.

I am thankful for Bill Burley for helping put together a weather balloon mission even though good weather never came.

I am thankful to Rob Young and Christian Hornhuber of the Instrument Design Lab for working with me towards solutions and making those solutions a reality.

Beyond the world of academia, I've always tried to love and value my family. I know academia has stolen me away from you all for too long, but such is the current way of the world. In retrospect I've realized how much their support contributed to driving me out of my low point in high school to my current standing.

I am thankful to my mother Gina Madison/Jacquart who is the best mother anyone like myself

could ask for. My mother has been there for the worst and best moments. There is little she would let keep herself or myself from our dreams. My mother exposed me to computers, and their power, early in life, likely shaping my affinity for them. My mother is better than your mother and I will fight you over it.

I am thankful to my father Todd Madison for being my original inspiration into the world of science and engineering. For being the characterization of a indomitable yet skeptical man in a world filled with those who seek to subjugate and exploit them.

I am thankful for my brother Tanner Madison who is simultaneously the best and worst brother. Through our fights and friendship, we can push and pull each other along; in this I value our time together.

I am thankful to my Grandmas Connie and Anita for believing in me. I hope that I can continue to make them proud.

I am thankful for my Aunts and Uncles, Earl, Jana, Nichole, Tim and, Robin. They have shown me the world and how to be an adult in different facets. My time with the last two, Tim and Robin, was not enough and, in a perfect world, they would be here to share in more of life.

I am thankful to my numerous cousins for being supportive and accepting. Especially my cousin Jackson whose adoration I do not deserve and who, I hope, can show the world his genius.

I am thankful to my stepparents. By my mother I am thankful for Rollie for accepting me into his home and family and tolerating me and our contrasting views. By my father I am incredibly thankful for Martina who has repeatedly supported me over the years in a way that one would expect of their own mother.

Lastly, I am thankful for the doctors of Children's Mercy Hospital, without whom I would have likely perished and never been able to experience anything beyond my youth.

Contents

List of Figures

List of Tables

Chapter 1

KUbeSat-1 Mission

1.1 Context

KUbeSat-1 is aimed to be the first successful CubeSat mission from the University of Kansas. This plays a role in NASA's 2014 White House initiative of 50 CubeSat missions in 50 states in 5 years (Mahoney, 2014). While this is a White House initiative, it faces considerable difficulty because each mission must be done independently. This is to say, without the assistance, financial or otherwise, of the federal government or its agencies for simply being accepted as a CubeSat mission. There are programs for financially assisting CubeSat missions, but they are not guaranteed and, as of this date, KUbeSat-1 was denied any such funding. To remedy this hardship the KUbeSat-1 mission has turned to both internal funding, from the University of Kansas endowment, and external funding, most notably from a sponsorship with PepsiCo (Peterson, 2019). The KUbeSat-1 mission has also worked with Tyvak Nano-Satellite Systems, whose President is a University of Kansas alumnus who lead a prior University of Kansas attempt to launch a CubeSat which failed during launch (Rombeck, 2005) (Tyvak, 2020). The KUbeSat-1 mission has been given a 3U CubeSat, but has been blocked from any further assistance, monetary or development wise from Tyvak. The KUbeSat-1 mission will have to construct its own satellite operating system, install its own power management system among other standard satellite subsystems. It will also have to develop its own ground stations and telemetry, since the standard ground stations and telemetry of NASA are not something that can be used per the original White House initiative requirements. The difficulties also extend to the payloads, wherein none of the Aerospace funding can be diverted to payload development, so all payload development must be done on independent funding and expertise. This

means that, for the payload lead, they must attain their own funding, construct entirely original research, instruments, data acquisition, and analysis methods. As a part of funding the Aerospace Engineering side has also started a kick starter using KU's LaunchKU system (Prinsloo & et al., 2020).

In the remainder of this section we will investigate some of the engineering physics important to the KUbeSat-1 mission and its payloads. KUbeSat-1 will fly on a Circular Sun Synchronous Orbit (SSO) with an orbital period of 93 minutes and orbital height of 500 ± 50 kilometers. The orbit inclination will be roughly 90 ± 5 degrees and the eccentricity will be roughly zero. This orbit was chosen as it guarantees a pass over the polar regions every 93 minutes, said regions being mostly radio quiet and where existing and future radiometric particle physics experiments exist. It is also where the most particle flux is expected, which is important for ensuring continuous and calibrated operation of any particle detectors. The orbit will naturally precess by roughly 0.986 degrees per day, as it stays Sun synchronous, and thus can effectively scan the surface of the Earth. This precession corresponds to roughly 110 km on the surface of the Earth, meaning that any such scanning device will need a beam width sufficient to scan that distance. Otherwise there will be dead zones, i.e. lower power zones, where the satellite signal does not reach. For the given height this corresponds to a minimum beam width of 13.7 ± 1.2 degrees. To estimate the power needed to be seen at Earth use the characteristics of most radiometric particle experiments exist; these experiments exist near 300 Kelvin and around 1 GHz of bandwidth, corresponding to a thermal noise floor of 4.14 picowatts. These experiments trigger optimally above 5 to 10 Signal to Noise Ratio (SNR). Treating 10 SNR as a minimum signal power gives 41.4 picowatts. Integrating over the bandwidth of 1 MHz to 1 GHz for the following Friis transmission loss:

$$P_{Rx} = G_{Rx} G_{Tx} P_{Tx} (\frac{c}{4\pi d})^2 \frac{1}{1GHz - 1MHz} \int_{1MHz}^{1GHz} \frac{1}{f^2} df = 0.57 G_{Rx} G_{Tx} P_{Tx} \frac{1}{d^2} \tag{1.1}$$

The distance, d, will correspond to the orbital height. The antenna parameters of gain of the transmitter, G_{Tx}, and receiver, G_{Rx}, are set to unity here for simplicity and for a minimal estimation. A factor of $\frac{1}{2}$ is included as the beam width definition is the section of the antenna's main lobe that

is above half-power. Thus, the minimum is a target that is on the edge of the beam and receiving half-power. Solving for the transmitter power, P_{Tx}:

$$\frac{1}{2}P_{Tx} = 1.7d^2P_{Rx} \rightarrow P_{Tx} = 3.5d^2P_{Rx} = 7.1 \times 10^{11}P_{Rx} \tag{1.2}$$

Results in a transmitter power of 29.4 ± 6.6 Watts integrated over 1 MHz to 1 GHz. This assumed a flat power spectrum for both antennas, which is likely not true and underestimates the power. This also assumes no extinction from media between the transmitter and receiver; there is minimal extinction in the atmosphere and parts of Earth's upper crust in this bandwidth. We also require that the Attitude Determination and Control System (ADCS), which determines and controls how the satellite is configured in space at any time, must be accurate within the beam width. For KUbeSat-1 this is possible as the 5σ attitude precision is 0.215 degrees and pointing precision of 0.285 degrees. The star tracker of KUbeSat-1 has a Pitch/Yaw/Roll a 5σ precision of 0.111 degrees. Thus KUbeSat-1 should be capable of any Earth scanning experiment in terms of orientation. This leaves one element, how to generate a roughly 30-watt signal on a satellite with a maximum power generation of 5.8 Watts per orbit. Clearly a continuous wave signal would then be impossible as there is not enough power. Instead a pulsed signal is used so that the average power can be lower than 5.8 Watts, but the instantaneous power can be 30 Watts. With a pulsed signal the orbital velocity of the satellite then must be considered as, if the pulse rate is too slow, the satellite will have gaps in coverage. At the given orbital period the corresponding angular velocity is 0.18 ± 0.02 milli-radians per second. This may be slow but, the Earth is huge; the corresponding surface velocity is then 1.14 ± 0.12 $\frac{km}{s}$. Since the minimum beam width is already constrained by the precession of 110 km this also impacts the pulse rate with the velocity. The minimum pulse rate needs to be capable of achieving half the precession, or 55 km. This minimum pulse rate is then once every 39.29 ± 0.08 seconds. This is similar to the amount of time a satellite in low earth orbit (LEO) is visible from the ground as it is on the order of half a minute to a minute. With a lower end of the bandwidth at 1 MHz such a pulse would occur over 1 micro-second, giving an average power use of 29.4 ± 6.6 micro-Watts per pulse for a minimum power rate of 44.9 ± 10.1

micro-Watts per second. For an entire orbit this is a power draw of roughly 251 milli-Watts per orbit, which is within the acceptable range of operation of KUbeSat-1. This assumes that all the power used goes into the signal, which almost certainly wouldn't happen and, it is also ignorant of methods of generating signals that do not require directly using satellite power to generate signals. An example of the latter being piezoelectric sources.

The KUbeSat-1 satellite frame is made of aluminum alloy and measure 100 x 100 x 340.5 mm^3 and a usable side-length of 80 mm. This constitutes the 3U frame, weighing in around 450 grams. Within this frame sits the satellite bus, the ADCS, the power control system, the communication system, and the payloads. Further specifications of interest for this discussion are the voltages available, being 3.3V, 5V and 12V, a 1W heater system to climate control the satellite, and a UHF band communications system which can telemeter data at a rate of 1-250 kbps. For those who are fans of operating systems, the operating system for the bus is MINIX based.

1.2 Brief History of Payloads

To date the KUbeSat-1 mission has had multiple proposed payloads as it proceeded towards launch and determined specifications. Brief discussion of the payloads, how they've changed, and if they have been cut follows.

1.2.1 Fundamental Technologies Energetic Particle Detector

Shortened to FTEPD, it was designed to measure the difference in downward and upward flux of charged particles and ions during orbit. The energy range was a few eV to a few MeV. This was planned to be done using a combination of solid-state silicon detectors and avalanche photodiodes. There were two sides to this detector, a top upward facing and a bottom downward facing. The motivation for this payload is that there are not sufficient nor recent measurement of particle flux in LEO. By not having these measurements it is harder to prepare LEO payloads and simulation of LEO satellites are less accurate. The signals of both sections were to be read out to a high

sampling rate ADC. Alongside the Primary Cosmic Ray Detector (PCRD) this would have been able of measuring correlations in upward and downward ion flux with primary cosmic rays. The FTEPD did not become a KUbeSat-1 payload.

1.2.2 Astro-Biology Cultures/Calorimeter

Shortened to ABC, it started as a combination of experiment and outreach program to bring fungal cultures, and their potential Astro-Biological utilities, to classrooms and to KUbeSat-1. ABC was a part of multiple student projects over the years, including a weather balloon launch. At one point it was explored as a possible calorimeter, wherein the potential/pH of a fungal culture would be read over time as the culture experienced radiation. This is possible as the respiration of many fungal species correlate to the production of acid, particularly in the case of the radiation hardened and space capable Aspergillus Niger there is a significant production of citric acid. ABC did not fly on KUbeSat-1 as the primary student working on it was already devoted to two other payloads and did not have time to devote to a third payload.

1.2.3 Primary Cosmic Ray Detector

Shortened to PCRD, this payload is a result of a chapter research application at KU Physics and Astronomy's Society of Physics Students (SPS) chapter (Lubis et al., 2017). After winning this award and the related funding most of the SPS participants moved onto other projects or schools. Around this time the focus and methods of the PCRD changed frequently, partly because the students involved did not fully understand the possible hardware or physics objectives that a cosmic ray detector on a CubeSat could have. As the name suggests the overall theme was to measure primary cosmic rays, consisting mostly of protons and being only accessible from space. After more thought the PCRD was incorporated into the Anomalous Cosmic Ray Experiment (ACRE) as one of the two detectors in the ACRE payload.

1.2.4 High-Altitude Calibration KUbeSat

Shortened to HiCalK, is a continuation of the previous HiCal experiments that were done in collaboration with the ANITA experiment, which looks at radio emissions by Ultra-High-Energy-Cosmic-Rays (UHECRs) (Gorham et al., 2017). Said HiCal-1 and HiCal-2 experiments used a secondary weather balloon, a pressure vessel containing a piezoelectric sparker and bicone antenna to send RF pulses towards the ANITA experiment for the purpose of calibration and surface reflectivity measurements. This was extended to a CubeSat platform for the purpose of having a dedicated and long-term ANITA transmitter source. It was soon realized that, with a Sun Synchronous orbit, this could effectively help calibrate any radio based UHECR experiment. The initial design involved using the pre-existing bicone antenna and piezoelectric pulser. This was an issue as the bicone antenna had dimensions greater than the size of KUbeSat-1 and because, at the time, the piezoelectric pulser was believed to require an electrostatic discharge (ESD) and thus would require at atmospheric chamber within KUbeSat-1. The leadership of HiCalK changed multiple times until the author became the leader, and current leader. Under the current leader the bicone antenna was removed for an antenna small enough for KUbeSat-1 and with similar, if not superior, performance. The pulser was also tested and it was confirmed that the piezoelectric pulser did not need ESD to generate an RF pulse.

1.3 Environment in LEO

1.3.1 Particles

LEO has different definitions depending on the purpose. One consensus is that the transition of LEO to Medium Earth Orbit (MEO) is at 2000 km. LEO serves as a unique platform for Particle Astrophysics as it is below the typical altitude of the inner Van Allen belt, 1000 km, and above the denser parts of the atmosphere. A graphic indicating these orbits can be seen in Figure 1.1.

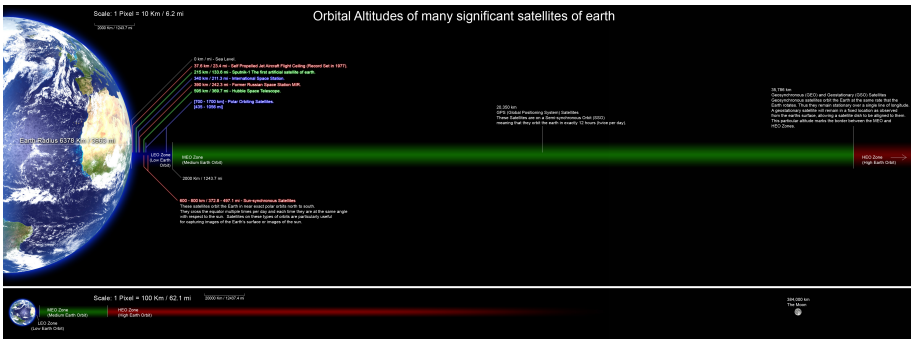

Figure 1.1: Graphic of orbits as they get further from Earth's surface. Despite the figure indicating that Sun Synchronous orbits occur in a specific range, this is not true. It is possible to achieve Sun Synchronous at other altitudes by modifying the eccentricity. Image credit to wiki user Rrakanishu.

The dominant particle background is primary cosmic rays (PCR) that are usually treated as traveling down towards the Earth but are mostly isotropic. This is to contrast with secondary cosmic rays (SCR), the kind of cosmic rays seen at the surface of Earth which result from interactions that PCRs have with the atmosphere and are thus downwardly biased. The majority of PCR, by a few orders of magnitude, are protons. Secondary to PCR are Solar Energetic Particles (SEP) that make most of the solar wind coming from the Sun. SEPs mostly consist of low, near keV energy, electrons but also include protons and ions. SEPs travel outward from the Sun but can be pulled down toward the Earth by the Earth's magnetic field. Lastly, in the rare cases when the inner Van Allen belt drops, there can be upward and downward fluxes caused by the movement of charged particles due to the inner Van Allen belt, which will be referred to as Van Allen particles (VAP). These phenomena also span different energy ranges where PCRs have a most probable value around 1 GeV or so. The VAPs are around 100 keV for electrons and around 100 MeV for protons in the inner belt, most of which are thought to be trapped SCRs and SEPs (Tascione, 2004). For SEPs the energy range that must be considered is much larger as the overall number of SEPs is about 10^{10} higher than PCRs. The most probable energy of SEPs comes from constant solar wind and is roughly 1 keV (Mewaldt, 2001). For more energetic emissions by the Sun, such as flares and Coronal Mass Ejections, SEPs can reach many MeV or GeV. These events are rare though, and these SEPs would be indistinguishable from PCRs. One important comparison is that the flux of SEPs at 1.0 MeV is roughly the same as the flux of PCRs at 1 GeV (Group et al., 2019).

This is to say, by 1 GeV SEPs are many orders of magnitude less likely than PCRs. To check this against a second reference the space environment simulator used by the European Space Agency (ESA), known as SPENVIS, was used for an orbit falling within the KUbeSat-1 parameters. The result for particle flux, as seen in Figure 1.2, integrated for the cross-section of a CubeSat (10 cm^2) gives a total rate of 1021.3 events per second for nuclear particles and 1.74 events per second for electrons.

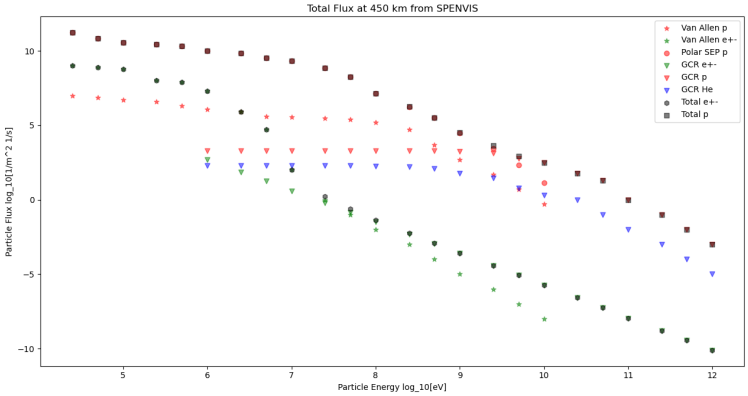

Figure 1.2: Total particle flux in a LEO, particularly 450 km SSO. This diagram may be misleading as the flux due to SEPs and Van Allen belt particles are largely dependent on the satellite being within a region of space where the magnetic field is weak enough, or has changed direction, to allow said particles to pass through LEO.

This integration is misleading as most of the time VAPs and SEPs occur only in regions of orbit with localized magnetic fields that allow them to exist, as seen in 1.3. Note that SPENVIS uses the AE-8 and AP-8 models to generate the flux of VAPs (Sawyer & Vette, 1976) (Vette, 1991). Said models are by no means perfect and are somewhat outdated due to the lack of new data and limited scope of previous data.

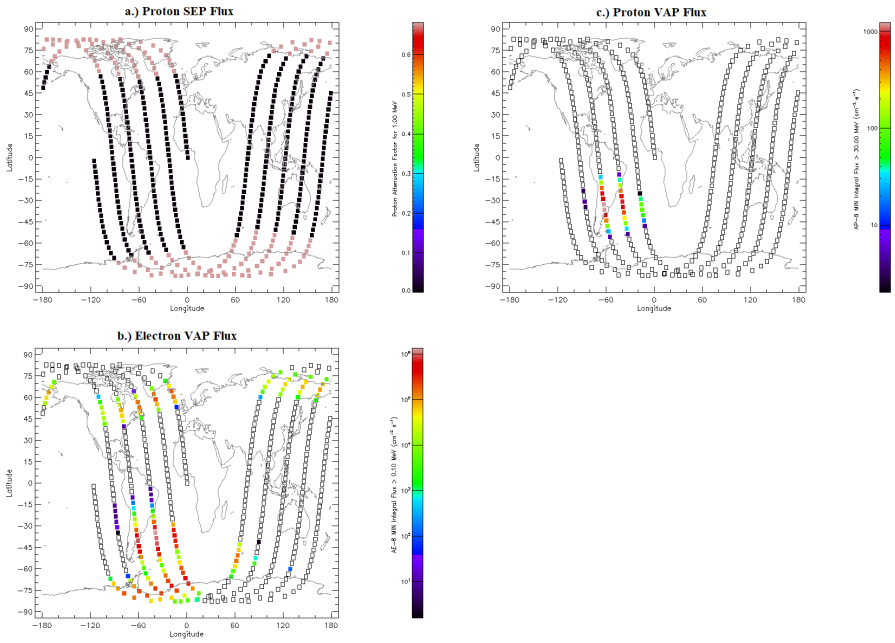

Figure 1.3: Particle flux in five orbits of a LEO, particularly 450 km SSO. Plotted on a Lat-Long map. By plotting on a map, it is easier to see the time and spatial nature of the particle flux. In particular the equatorial regions are typically quiet of non-PCR flux.

Removing this yields that, in polar regions the rate will be 1020.8 nuclear events per second and 7.4×10^{-6} electron events per second, in VAP regions there would be 0.67 nuclear events per second and 1.74 electron events per second. Outside of both of these regions the event rate is dominated by PCRs with 0.14 nuclear events per second and 7.4×10^{-6} electron events per second. Some skepticism is needed in these results as SPENVIS does not have flux for electron SEPs. This may be because they are often 1 keV or lower unless there is significant solar or auroral activity (Wilson & al., 2016). Still, this indicates that outside of noisy regions of space that having an electron and nuclear event occur simultaneously, and having electronics which can resolve these events within 10 μs or so, would give a coincidence rate of 1.04×10^{-11} or 0.33 events in 1000 years. Such an event signature would then be fairly rare for a CubeSat mission that lasts six months to a year.

1.3.2 Plasma

There are various kinds of plasmas that exist in LEO, in both trapped and free moving forms. One global plasma is the ionospheric plasma which, at LEO, consists of the F region. The F region comprises of different layers of plasmas of various ionized particle species, dominantly O^+ but also O_2^+ and NO^+ (Kamide & Chian, 2007). These layers can merge and disassociate based on solar activity, daytime vs. nighttime, but they are mostly trapped in their region of space. They are classified as low density and hot plasmas as the density is roughly 1×10^12 particles per cubic meter and the temperature is roughly 2000 K (Brace & Spencer, 1963). For the purpose of spacecraft, the F region can cause interference in radio communications, increased atmospheric drag and damage to space craft electronics, all due to ionospheric charging. During charging electronics can arc, short out or ground out depending on how the charging occurs. All of these can contribute to satellite failure. Similar plasmas can exist in the polar regions of Earth but in both free and trapped forms. Geomagnetic storms may occur as Earth's magnetosphere responds to solar radiation. Geomagnetic storms last days and cause significant flux of particles through the polar regions. These storms can have localized plasma manifestations in the forms of auroras, substorms or Strong Thermal Emission Velocity Enhancement (STEVE). An image of a STEVE can be seen in Figure 1.4.

Figure 1.4: Image of a STEVE where multiple plasma species can be seen due to the color and spatial differences in the STEVE jet. Photo taken by Hans Howe above Lake Superior in Michigan, United States.

In the case of STEVE a jet of multiple plasma species, ions and electrons, develops and travels at roughly 6 km/s across hundreds to thousands of kilometers over the course of a few hours to a day (Gallardo-Lacourt et al., 2018). The density of STEVE is roughly 1×10^{13} particles per cubic meter and temperature is roughly 5000 K. This makes STEVE arguably the most extreme plasma event that occurs in LEO. Considering this and other plasma interactions NASA Engineering and Safety Center (NESC) has recently worked on developing a computation model for these plasmas and how to better prepare and combat them (Hamm & al., 2019). There have been no efforts to recreate a STEVE-like environment and to test spacecraft and/or electronics in said environment, but this may be due to the relatively recent development in concern over plasmas in LEO.

1.3.3 UHECR Air Showers

As briefly discussed earlier in section (B5), UHECR can cause air showers wherein thousands to millions of shower particles are generated. Normally these are investigated on Earth by looking at downward air showers. This does not mean that cosmic rays are all downward particles;

measurements by Pierre Auger Observatory suggest mostly isotropic with minor anisotropies in the direction of energetic astronomical processes like gamma ray bursts (Aab et al., 2018). It is expected that there are air showers that are upward or "Earth grazing" that only penetrate the atmosphere and not the Earth itself. Such showers would be capable of escaping the atmosphere once they are above roughly 50 km as the interaction length above this altitude becomes comparable to the altitude of LEO and the energy loss becomes comparable to 1 $\frac{eV}{km}$. Some components of these showers and other cosmic ray interactions are anticipated as parts of the inner Van Allen belt flux but it is currently inconclusive what fraction this process would contribute, or what the flux of these particles at LEO would be [10]. The solid angle for these upward showers from LEO is also considerable as following the solid angle calculation:

$$\Omega = 2\pi(1 - \frac{\sqrt{2(R_E + \tau_{atmo.})h + h^2}}{R_E + \tau_{atmo.} + h}) - \Omega_E \tag{1.3}$$

Where the radius of Earth is R_E, the solid angle of Earth with respect to the satellite orbit is Ω_E at an orbital height of h and an atmospheric thickness of $\tau_{atmo.}$. At a 450 km orbital height this value is 46898.5 km^2 which is a considerable area to integrate over as it corresponds to roughly 46.7 million events per second, all with thousands to millions of shower particles. This is assuming that cosmic ray flux is truly isotropic, which, as discussed before, is a commonly accepted approximation.

Chapter 2

PCRD

2.1 Objectives

There are two main objectives to PCRD, to measure primary cosmic rays, the dominant background, and to do so in a way that can be applied to future missions. The particle objective is further specified for this mission by horizontally propagating particles above a few MeV. The most recent benchmark experiments for measuring comsic rays, AMS and PAMELA, did so with vertical propagating geometry, so PCRD hopes to contribute to these measurements by changing direction it is sensitive to (Aguilar et al., 2013) (Adriani et al., 2017). PCRD will feature shielding such that it will focus on the high energy physics (HEP) component of space particles. These are then identified by a particle identification (PID) technique using pulse shape discrimination (PSD). From this PCRD will be the first HEP CubeSat payload from a public American university and first CubeSat payload to use pulse shape discrimination (Kulu, 2020). Achieving will set the ground work for future large scale HEP experiments, such as 100 or more CubeSat and PCRD array in LEO, that could be the largest volume HEP experiment ever created. It would also have access to UHECR, the highest energy particles known to exist. Thus, this proof of concept is crucial.

2.2 Geometry

The initial geometry of the PCRD was to have multiple scintillator paddles stacked vertically, but this was abandoned as a vertical stack would cause issues. Notable among these issues are contamination wherein a downward cosmic ray which penetrates all the paddles would be indistinguishable

from an upward cosmic ray. This issue is extended further when the other scintillator paddles are made of scintillators that detect different particle species as a downward cosmic ray could produce, for example, a delta ray which triggers an electron scintillator and then, by itself, trigger the PCRD. This signal is then identical to an upward cosmic ray that produces a delta ray. Therefore the scintillators were rotated to be on their side such that all scintillators are preferentially triggered by horizontally propagating particles, which, as seen in the angular spectra in Figure 2.1, is the dominant direction for low energy shower protons (Pazianotto et al., 2018). Since horizontal propagation, with respect to Earth's surface, is also the direction of the Earth's magnetic field there is minimal Lorentz force for North-South horizontal propagation. For East-West horizontal propagation the magnetic field will curl particles upward and downward. For a 10 GeV proton the gyroradius would be nearly 1 km, meaning these particles should be trapped in the atmosphere. Similarly, Up-Down particles will curl East-West into circles of similar gyroradius. Thus, there should be more horizontal triggers along the North-South direction, which is thusly the orientation of the two coincident detector sections.

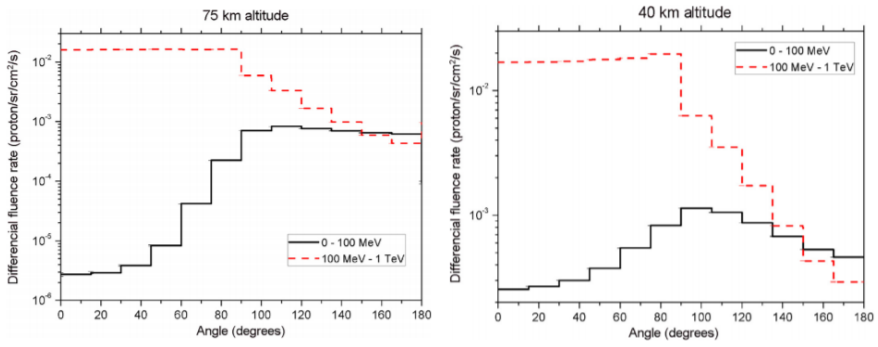

Figure 2.1: Angular distribution of UHECR shower protons as a function of angle and as the depth of the shower increases. The trend indicates that the deeper the shower the wider the angle of the shower particles become. This angle is the zenith angle, not the angle from the primary cosmic ray, and was the result of an average of a Monte Carlo simulation of isotropic cosmic rays.

The orientation of the scintillators will be held constant by the reaction wheel and torque coil on the KUbeSat-1. The background is further suppressed as, show in section C1.), the coincident flux of two cosmic rays of different species is essentially zero across the lifetime of the KUbeSat-1 mission. The population of downward shower SCRs would also be expected to be essentially

zero at LEO as the density of the atmosphere is nearly 10^{-10} of sea level density and thus the interaction length, which is the typical length needed for shower population to double, of roughly 370 $\frac{kg}{m^2}$ gives a distance of $\approx 3.7 \times 10^{10}$ kilometers. This distance becomes physically attainable once downward cosmic rays go to denser parts of the atmosphere. To hold the detectors in place and shield against lower energy particles shielding and mounting is needed. This shielding, and by extent the detector, are constrained by the 1U (i.e. 10x10x10 cm^3) and 1 kg limits of a CubeSat. In addition to this there is a railed mounting system that constrains this down to 8x8x8 cm^3. As there is also space needed for cabling for signals to be sent to the satellite bus to be telemetered this is reduced further to a 7x7x7 cm^3 volume. Using these constraints, and that coincident detectors will need four cables on both sides, the schematic given in Figure 2.2 was designed.

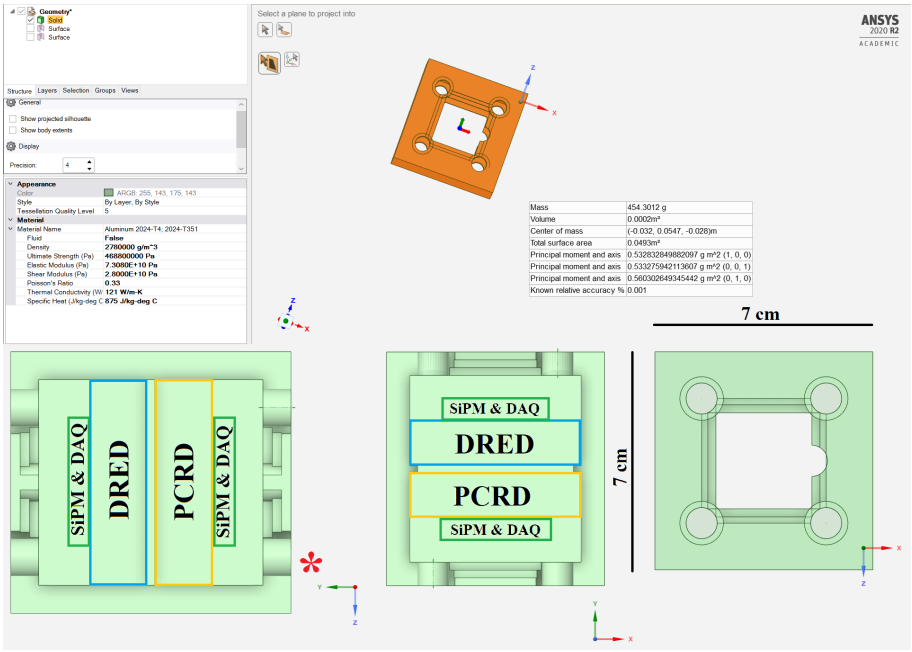

Figure 2.2: CAD representation of the ACRE shell which house PCRD and DRED. The red star denotes the orientation that the shell will have while perpendicular to Earth, i.e. the flown orientation. There is an opening on either side to allow for the putting objects inside that will have lids that match the terracing of said opening. For machining and assembly purposes this shell has been revised multiple times but the original image is kept here as a reference.

The mass of this shell design is 454 grams and is acceptable for mass constraints. The scintillators will have a combined mass of roughly 134 grams and circuitry will have a mass of roughly 125 grams. This puts the total mass below the 1 kg constraint. The thickness of this shielding is 0.75

millimeters which corresponds to an electron threshold of roughly 1 MeV and proton threshold of roughly 15 MeV by using data from the PSTAR and ESTAR databases (NIST et al., 1998) (NIST, 1998).

2.3 Scintillators

One way of detecting particles, particularly for counting, is by using scintillators coupled to photomultipliers. A scintillator is a material that, when an energetic particle, above a minimum ionization energy, passes through it causes ionization within the scintillator. These ionizations are related to the material being used. For PCRD the scintillator is an organic scintillator comprised of Poly-Vinyl-Toluene (PVT). The light output of organic scintillators can be controlled by changing the ratio of hydrogen, oxygen and carbon, mainly through adding chains of Benzene rings. Tertiary doping elements, like Boron and Lithium for neutron scintillators, can also be used. Phosphorous compounds like Silver activated Zinc Sulfide (ZnS:Ag) can also be used, particularly on the surfaces of the scintillator that face the incoming radiation. For organic scintillators one of the most important parts are Benzene rings which have chains of π electron states. As these chains increase in count the π states effectively increase in size and red shift their emission wavelength as well as their ability to absorb energy, particularly UV ionization energy (Friedel et al., 1952). Considering this Anthracene and Tetracene, being three and four chain Benzene rings, are added as doping agents in organic scintillators. There are also π Donor-Acceptor interactions between the Benzene rings' π electron states and the lower energy π electron states of doping compounds wherein π electrons can be exchanged and lowered to even longer wavelengths before being emitted. These properties allow organic scintillators to not only absorb high energy radiation and re-emit it at wavelengths detectable by photomultipliers but also allow for the construction of wave length shifters where light of shorter wavelengths are absorbed by high energy aromatic π states (meaning similar to Benzene) and then donated to either lower energy aromatic π states or non-aromatic π states and then emitted at the longer wavelength. Since the decay times of π states can also be tuned based off the chemical structure in question it is possible to use these aromatic compounds

to change the decay time of radiation. By shifting the decay time to a longer value the quick ionization of particle radiation or emission of a small decay time scintillator can be shifted down to long decay times that are detectable by lower sample rate electronics.

There are three important characteristics for scintillators, the light yield typically quoted as a percentage of a standard scintillator, the density and, the time constant of the ionization. The light yield of a scintillator in terms of the $\frac{dE}{dx}$ value can be derived using Birk's Law, which uses Birk's constant k_k and the scintillation efficiency, S, of the geometry in question:

$$L = S\frac{\frac{dE}{dx}}{1 + k_k \frac{dE}{dx}} \tag{2.1}$$

As an example, for a 1 GeV Muon passing through 1 millimeter of a PVT scintillator this value is roughly 88 keV of deposited energy. To contrast this to a similar detection process, Cherenkov radiation has an intensity, $I = \frac{d^2E}{dxd\omega}$ that can be determined by the Frank-Tamm formula (Frank & Tamm, 1937). Wherein:

$$I = \frac{Z^2 e^2 \omega}{4\pi} \mu(\omega)(1 - \frac{1}{\beta^2 n^2(\omega)}) \tag{2.2}$$

The number of charge of the impending particle is Z with its velocity as a fraction of light speed being β as it travels through a media of refractive index $n(\omega)$ and permeability $\mu(\omega)$. From this it is seen that Cherenkov intensity does not depend upon the density of the media, the intensity prefers higher frequencies, is asymptotically dependent on the particle's velocity and, there is no time constant for the radiation. As such Cherenkov radiation received at a photomultiplier is expected to be similar to a delta-function as there is no decay time but instead a finite width associated to the geometry of the detector and the response characteristics of the photomultiplier. Assuming minimal changes in permeability and index of refraction and integrating over the frequency band that is viewable by the photomultipliers being used, here PM33 with a bandwidth of 0.33×10^{15} Hz to 1.0×10^{15} Hz is used (KETEK, 2019). These factors yield:

$$\frac{dE}{dx} = (2710\frac{eV}{cm})Z^2(1-\frac{1}{n^2\beta^2}) \tag{2.3}$$

This value is considerably smaller compared to the 880 $\frac{keV}{cm}$ calculated for loss from ionization (PDG et al., 2019). There have been experiments that have separated these signals by using scintillators with long time constants, such that the Cherenkov peak is not masked by the scintillator peak. A demonstration of this can be seen in Figure 2.3 where the scintillation and Cherenkov signals received by a photomultiplier coupled to a scintillator were separated (T. Kaptanoglu and M. Luo and J. Klein, 2019).

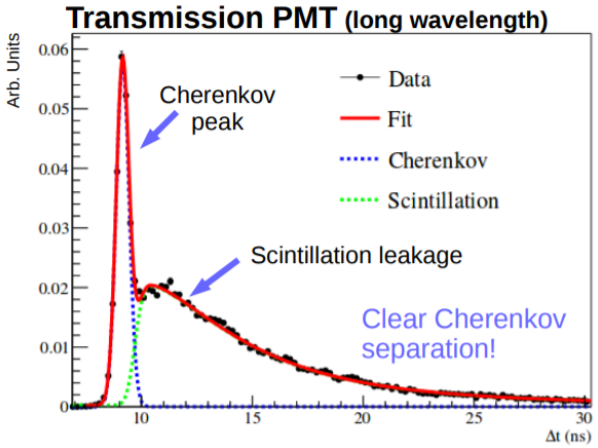

Figure 2.3: Figure as presented by T. Kaptanoglu et al. wherein scintillation signals from a liquid scintillator and its Cherenkov radiation signals where separated. The fit values for the Cherenkov radiation were done using a width parameter and the scintillation radiation was fit using the scintillator decay constant.

In many cases particles will be high enough energy to create both Cherenkov radiation and scintillation radiation. The reason for this is due to both the index of refraction of most scintillators being around $n = 1.5$ and the velocity threshold for Cherenkov radiation being $\beta_{thres.} = \frac{1}{n} \approx 0.67$. This gives a Lorentz factor of roughly 1.35. As such an electron with 0.688 MeV, muon with 143 MeV, proton with 1263.5 MeV, would all produce Cherenkov radiation while all particles above 1 keV or so would release detectable scintillator radiation (PDG, 1999). One caveat to this is that the minimum energy for scintillation detectors can instead be determined by the shielding, if it exists, as particles will have to pass through the shielding to get to the scintillators; shielding can be used

to control the effective energy threshold of scintillation detectors. To shield out lower energy electrons, which are plentiful in LEO, 0.75 cm of T4 aluminum shielding is used. A scintillator with a long time constant, namely a BC444 equivalent, will also be used. Using BC444 advantageous for separating Cherenkov and scintillation radiation and its longer time constant is easier to integrate and trigger on for the lower frequency hardware that is accessible to CubeSat missions. A calibration run was conducted using cosmic ray muons. A ratio of energy deposited to integrated voltage and peak voltage detected at the photomultiplier can be attained by averaging over a sufficiently large data set. This is possible as the energy deposited by muons is already well characterized. Even without this ratio the ratio of energy deposited by Cherenkov radiation and scintillation can be attained. We propose this ratio be written in terms of decibels (dB) as the radiation gain, $\mathscr{R}$:

$$\begin{aligned}\mathscr{R} &= 10\log_{10}\left(\frac{L}{\frac{dE_{Cher.}}{dx}}\right) \\ &= 10[\log_{10}\left(\frac{dE_{scint.}}{dE_{Cher.}}\right) + \log_{10}(S) - \log_{10}(1 + k_k \frac{dE}{dx}_{scint.})] + \varepsilon \\ &= 10\log_{10}\left(\frac{P_{scint.}}{P_{Cher.}}\right)\end{aligned} \tag{2.4}$$

The energy deposited is usually written as $\frac{dE}{dx}$ but since these integrate over similar distances the denominators are omitted. The final values, in terms of the power of each signal, is what is measured at the photomultiplier. The photomultiplier is treated like an antenna receiving radiation from two different thermal sources and the radiation gain, $\mathscr{R}$, is the gain between them. An additional term, referred to as ε, represents the differences in efficiencies of the two forms of radiation as their quantum efficiencies will be different due to different wavelength content and response from the photomultiplier as well as having different geometric efficiencies due to Cherenkov radiation having a conical structure while ionization radiation is more isotropic. Since this requires a similar sample of the Cherenkov and scintillation power complicated scintillator geometry, particularly capable of focusing the power onto a silicon photomultiplier (SiPM), is needed. One also needs long decay time scintillators so that the Cherenkov and scintillation peaks can be differentiated. To do

this we propose paraboloid scintillators made of plastic scintillator material with longest possible decay time. From the reference characteristics of these scintillators $\mathscr{R}$ can be calculated from the expected Cherenkov and scintillation power. Using a reference pulse from an experiment which did a similar measure a value of $\mathscr{R}$ of 27.41 dB was found. This is close to the expected value of 27.85 dB for the Sr-90 β source they used and for the linear alkyl benzene (LAB) scintillators they used. The theoretical values for their setup, calculated from reference values, can be seen in Figure 2.4 (von Krosigk, B. and Neumann, L. and Nolte, R. and et al., 2013).

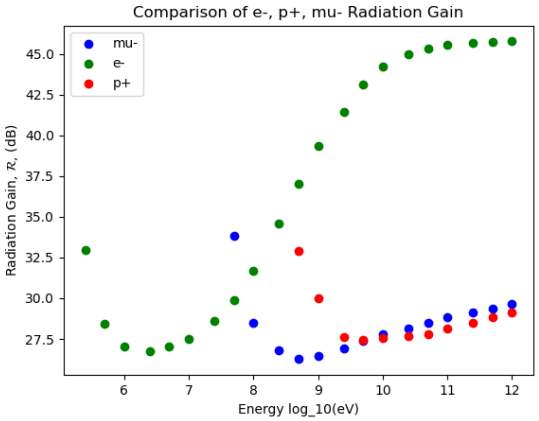

Figure 2.4: Ratio of ionization radiation to Cherenkov radiation in liquid LAB scintillator in terms of the radiation gain parameter $\mathscr{R}$. Values used in calculation, like the Birks constant and scintillation efficiency, taken from reference. This was calculated so that it can be compared to the $\mathscr{R}$ value calculated using the reference's Cherenkov and scintillation separated signal.

A similar feat was accomplished without the sophisticated setup the reference uses. Possibly indicating that the separation of these pulses may be easier when the photomultipliers are placed in the direction of the Cherenkov radiation, instead of perpendicular to it as is the case in the reference. With knowledge of $\mathscr{R}$, as well as the location in orbit, the particle species and energy can be further constrained. These constraints are done by using the Cherenkov radiation energy to constrain β, the location in orbit also changes the probabilities of each particle species and thus can constrain their likelihood, then the scintillation radiation energy can be used as a constraint on particle energy since β and the species are already constrained and scintillation radiation is dependent on both of these other constraints. To demonstrate this the same process was done with

SCR muon data taken in the lab, as seen in Figure 2.5.

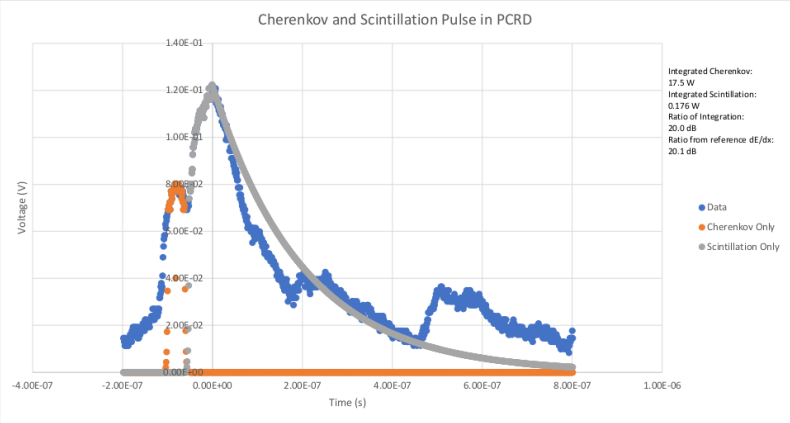

Figure 2.5: Double pulse from a cosmic ray passing through a BC408 scintillator. The Cherenkov and scintillation radiation have been separated so that their ratio can be found and then the ratio, $\mathscr{R}$, is found using both the values from data and the values from references.

The reference $\mathscr{R}$ was set using a 1 GeV Muon, which is roughly the average cosmic ray Muon energy. A $\mathscr{R}$ of 20.14 dB was expected but a value of $\mathscr{R}$ of 20.0 dB was measured, which may be further improved upon with more data and further modeling of $\mathscr{R}$ by improving the efficiency, ε, term which was set to 0.25 in this calculation. Considering that this explains both the reference, electron in LAB scintillator, and the data taken here, done with SCR muon in PVT scintillator, the $\mathscr{R}$ parameter seems promising. A comparison for different particles can be seen in Figure 2.6.

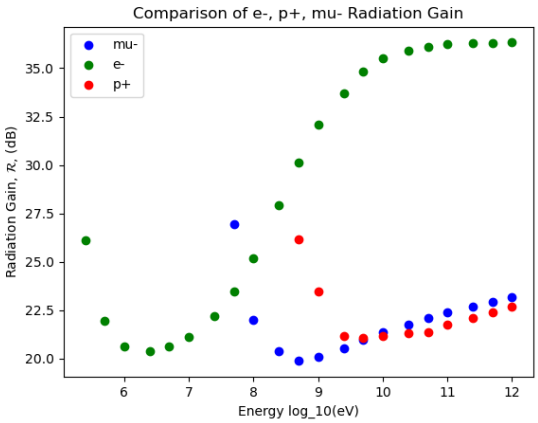

Figure 2.6: Ratio of ionization radiation to Cherenkov radiation in a BC408 scintillator in terms of the radiation gain parameter $\mathscr{R}$. Values taken from PDG, PSTAR, and BC408 references.

Each particle species has a relative neighborhood where their ratio minimizes as well as a minimum cutoff caused by Cherenkov radiation cutoff. Using $\mathscr{R}$ and the total energy deposited which is correlated to the power seen by the photomultiplier, seen in Figure 2.7, the particle energy and species can be constrained.

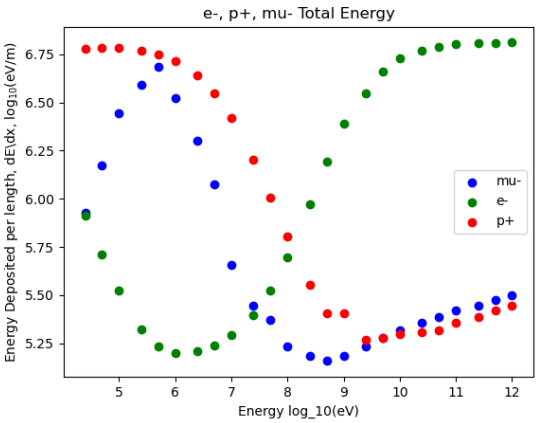

Figure 2.7: Total energy per length deposited in a BC408 scintillator after correcting for Birk's Law and adding in Cherenkov radiation.

Using both parameterizations and only looking at protons and electrons, the most common particles in LEO, signal topologies can be determined. A low $\mathscr{R}$ and low signal voltage could correspond to a low energy electron or high energy proton. This signal topology for protons is then biased by the higher background rate for high energy protons, and the shielding blocking

most of these low energy electrons. A high signal voltage and no $\mathscr{R}$ value, i.e. no Cherenkov radiation, would correspond to a low energy proton as the electrons of energies able to penetrate the shielding will always have Cherenkov radiation. The final signal topology would be for the lowest energy and lowest $\mathscr{R}$, which would indicate low energy muons. High energy muons would be indistinguishable from high energy protons and so have no unique topology. Low energy muons are not expected in LEO as they are expected to either not be produced in large quantities or to decay before attaining LEO altitude. If there is an anomalous and significant flux of upward or Earth-skimming UHECR air showers, wherein UHECR pass tangentially through the Earth's atmosphere, then high energy muons may be produced, but this needs to be investigated further. A full presentation of the expected signal topologies can be seen in Table 2.1 with the most likely particle, corresponding $\mathscr{R}$ and integrated voltage, as well as energy range.

PCRD Signal Topologies			
Radiation Gain, $\mathscr{R}$	Integrated Voltage	Most Likely Particle	Energy Regime
Low, 21-23 dB	Low	Proton	High Energy, >5 GeV
None	High	Proton	Low Energy, 5 GeV >E >10 MeV
Lowest, 19-21 dB	Lowest	Muon	Low Energy, 5 GeV >E >0.2 GeV
High, 27-36 dB	High	Electron	High Energy, >0.5 GeV

Table 2.1: Table of signal topologies for PCRD from the use of integrated voltage and $\mathscr{R}$. By using both of these parameters and a bit of the pre-existing knowledge of LEO it is possible to backout the particle species and energy range.

In addition to testing against other particle species, most importantly protons, this method also needs testing at other energies and more statistical significance. Nonetheless it provides a quick and low computational memory and processing method to infer particle data from scintillation signals.

2.4 Hardware

Development of hardware for CubeSat platforms is incredibly difficult as there are restrictions which exclude most hardware. These restrictions are on power consumption being less than 1 Watt, dimensions being less than 10x10 cm^2, being operable at low pressure and across 230-370 Kelvin. On top of this hardware which works for data acquisition of particle detectors, notable they must be fast and high sample rate, faster than 10 microseconds and greater than 10 MSps, excludes most hardware too. This last restriction mostly owes to high sample rate electronics often being reliant on supporting appliances, being fairly large in terms of size themselves, or being power hungry and temperature dependent. The five attempted solutions can be seen in Table 2.2.

Data Acquisition Method	Strengths	Weaknesses	Tested?	Failed?
Arduino ADC	1.) Simple	1.) Not capable of multiple inputs. 2.) Too slow to get reliable values. 3.) Too power hungry to have multiple. 4.) Fails under 0 deg. C	Yes	Yes
IDL Comparator Board	1.) Cheap (∼100 USD) 2.) Low power (∼100 mW)	1.) Ringing on signal made output unstable. 2.) Board failed to operate after a month of testing.	Yes	Yes
FPGA ADC	1.) High sample rate ADC (∼200 MSps) 2.) Versatile	1.) Complicated to code and use. 2.) Most power hungry (∼1 W). 3.) Takes up most space (∼10x10 cm^2).	Yes	Yes*
JFET Integrator	1.) Simple 2.) Cheapest (∼20 USD) 3.) Lowest power (<100 mW)	1.) Integrates out the peak and integral voltage values. 2.) Raises the time resolution to ∼1 ms.	Yes	No
KUbeSat-1 ADC	1.) Full control over ADC characteristics.	1.) Complicated electrical engineering. 2.) In development.	No	No

Table 2.2: Table of ADC methods pursued, tested and those which failed or are in development. Includes strengths and weaknesses.
*Failure of FPGA was not due to performance but due to lack of manpower and lack of FPGA curriculum.

The original solution, to use an Arduino and its ADC, is not feasible for many reasons. The Arduino ADC is capable of 10000 kSps and has a multiplexed ADC input, meaning that, while it is advertised as having multiple ADC channels, it only has one dedicated ADC that switches between each channel (ATMEL, 2013). As such it is not capable of handling two photomultiplier inputs, which is the minimum of the payload. It also fails to operate correctly at low temperatures, which was documented across multiple 200 Kelvin freezer tests as well as a weather balloon launch where the ambient temperature was expected to be near 240 Kelvin. With that said, if one runs the

Arduino at its fastest sampling rate, uses a specific bridge resistor value of 22 Ω and, lowers the analog references voltage, which controls the resolution of the ADC, then photomultiplier pulses can be measured as a single sample point. As this is one sample the measure is unreliable and only suitable for demonstration purposes. The prototype of this can be seen in Figure 2.8 where prototype scintillator and photomultiplier are in the black box beneath the Arduino. In this case the Arduino was powered by a battery and the photomultipliers were biased by a daisy chain of batteries.

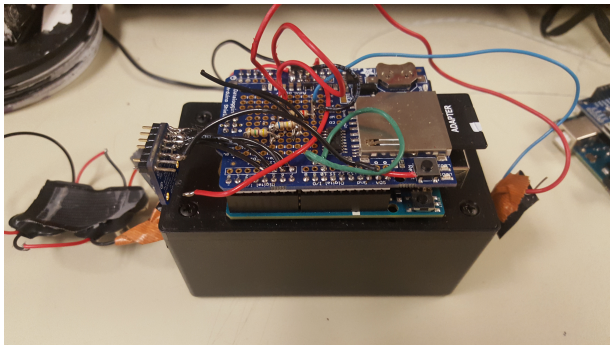

Figure 2.8: Arduino PCRD prototype. Data from the photomultipliers and the temperature sensor was saved onto the SD card shield for later analysis.

Following the Arduino prototype two paths were taken. One which was more complex and one more simple. The complex path involved using a Field-Programmable-Gate-Array (FPGA) and the XADC that some of the FPGAs have, particularly in the Artix-7 architecture. The X on XADC is proprietary and not of use discussing here. Programming an FPGA is no small task though as the programming language changes often, is mostly proprietary, and is a parallel programming language, differing from the serial programming languages like C++. This makes FPGA programming a much sought-after skill that is simultaneously impossible to develop. This logistical bottleneck also makes FPGAs under-documented and expensive. For the purposes of this test a Basys-3 FPGA learning kit was used. The Basys-3 is based off the Artix-7 architecture and has a 1 MSps XADC (DIGILENT, 2016). Once acquired the Basys-3 is programmable through Vivado HLS and a XADC program can be installed using the XADC wizard (XILINX, 2018). Using the example program the Basys-3 was capable of capturing a few points of each photomultiplier pulse,

which was then displayed on the Basys-3 number display so that it could be verified against an oscilloscope measurement in real time. An example of the amplitude of a photomultiplier pulse can be seen in Figure 2.9. Following this development of the FPGA was abandoned as, in order to make this capable of space flight, a custom FPGA board would have to be made and tested, which is well beyond the skills of anyone available to work or assist at the University of Kansas. As stated before, FPGA programming is much sought after and expensive, which heavily contributed to this outcome.

Figure 2.9: Picture of the Basys-3 display as it measured the amplitude of a photomultiplier pulse. Units are in volts, giving a reading of 98 mV.

For simple data acquisition there are comparators, which can be latched with a D Flip-Flop (D FF). The comparator has differential inputs and can be used to output a pulse should an input signal on one input pass the threshold set on the other input. The comparator's pulse is typically too fast for slow processors, like the ones on an Arduino, so a D FF can be used to create a latched pulse output. Some comparator architecture has built in latches but those can be problematic due to requiring hysteresis between the comparator output and the latch. Said hysteresis is also prone to ringing. These more complicated comparators often have higher input bandwidth too, which is problematic for this utility as it would accept more noise than what is desired. D FF also have reset pins, so once a microcontroller reads any D FF it can reset the array of D FF. The schematic for this design, seen in Figure 2.10, is fairly simple.

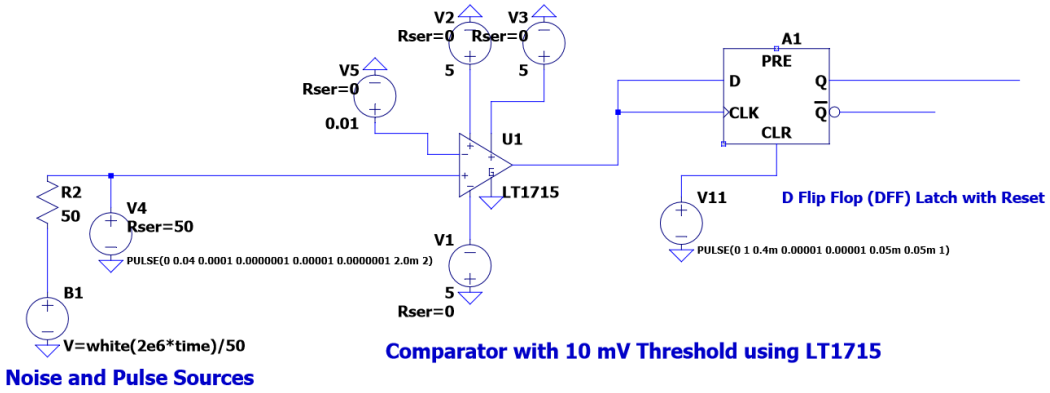

Figure 2.10: Schematic of the data acquisition circuit as simulated in LTSPICE. The photomultiplier signal was generated with white noise in order to generate a signal similar to the photomultiplier signal.

While this circuit is simple there was a need to use a hysteresis resistor for the comparators and bypass capacitors for the power supply rails for the comparator and D FF. In this schematic the threshold of the comparator is set to 10 mV. A presentation of the transient response of signals in this schematic can be seen in Figure 2.11 wherein the photomultiplier signal is latched by the D FF and then reset by an input simulating a microcontroller reset.

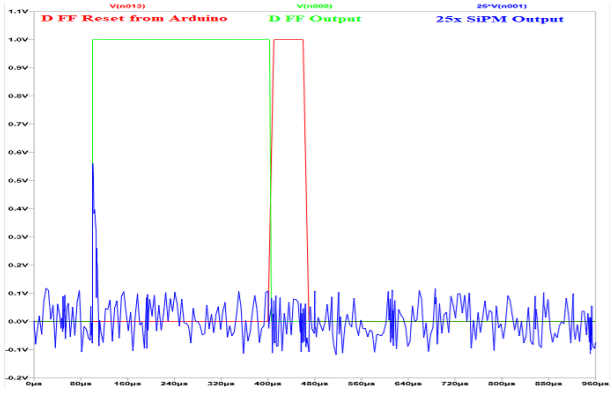

Figure 2.11: The output of the comparator is a square pulse that is roughly the width of the photomultiplier pulse and 5V in amplitude and is not shown. The photomultiplier pulse was multiplied by 25 times so that it would be recognizable next to the logic signals. The D FF latches the comparator signal and holds a digital high until a reset signal is sent. In this case the high signal is read by the Arduino and a reset signal (red) is sent which then drives the D FF low again. While the D FF is high any new comparator signal will be lost.

This circuit is also relatively low power and low cost. For one instance of this circuit the quiescent power consumption is roughly 40 mW and peak power consumption of roughly 200

mW. Each circuit has components costing roughly 5-10 USD depending on quantity and quality. This schematic was then sent to the University of Kansas Instrument Design Lab (IDL) wherein the design was further fleshed out and then two printed circuit boards (PCBs) were fabricated. In this expanded design four comparators and D FF were used. The schematic for the simulation and board can be seen in Figure 2.12.

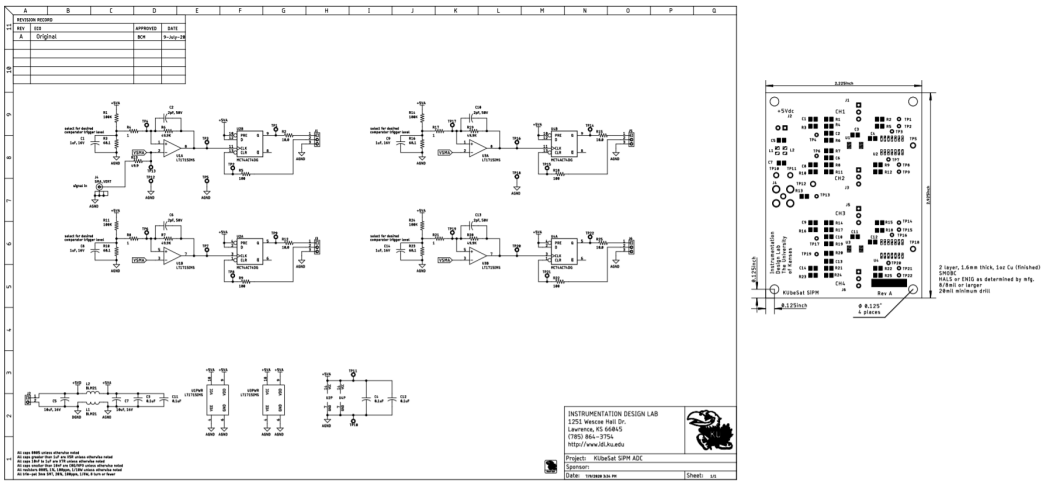

Figure 2.12: The circuit and PCB schematic for the comparator data acquisition board. There are four comparator channels which have different voltage thresholds that can be set with different resistor values for the voltage bridge on the comparator differential input.

This board worked in tests with signal generators but failed to produce consistent results with the photomultiplier pulses. This is for two key reasons. Firstly, the photomultiplier output is a semiconductor output and as such is not a controlled impedance signal. Most comparators are designed to sense controlled impedance signals and when they do not there is an impedance mismatch and therefore lots of signal reflections. Secondly, the circuit in this design has a hysteresis loop that shares a ground with the signal input. Normally this is fine but when the signal is now generating lots of reflections, particularly reflections that then go back onto the signal input ground, there are significant issues. These reflections can then travel to the hysteresis loop and trigger the comparator repeatedly. This produces comparator glitches, i.e. erroneous outputs, which would then set the D FF to high when it shouldn't be. It was also found that the two fabricated boards failed to operate after a month of testing, which is not acceptable for a yearlong mission in space.

The reason for this fail state seems to have come from all the comparator integrated circuits (ICs) failing at roughly the same time. This may have happened due to electrostatic discharge, but this is unlikely because the boards were kept in anti-static bags when not used.

In a attempt to produce a controlled impedance output for the photomultiplier that would better couple to the IDL comparator board, a controlled current voltage buffer amplifier was made using an n-channel JFET. It was found that by having a large enough RLC value this amplifier would behave like an integrator instead of an amplifier. The schematic for this can be seen in Figure 2.13.

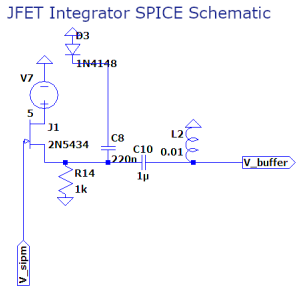

Figure 2.13: Voltage buffer integrator using a n-channel JFET. Original circuit design with the diode serving as both a high voltage protection and a high impedance current drain.

Actual values and parts used in the lab were similar but not identical to this schematic. This integrator has a mostly controlled output impedance of 1-10 kΩ compared to the 0-10 MΩ swings that a photomultiplier can cause. The integrator outputs a square pulse with a width and amplitude correlated to the width and amplitude of the original photomultiplier pulse. This integrated pulse is on the order of fractions of a millisecond in width, making the JFET integrator a slow operation data acquisition system. This operation is slow enough to be caught by slow ADCs like the kind on an Arduino, so this slower pulse may be useful for slower data rates and lower quality data acquisition. This slower rate has penalties in that the rate of false coincidences seen by the detector goes up as the time resolution of the data acquisition goes up. Increasing from a few microseconds to a few milliseconds effectively increases the rate of random, erroneous, coincidences by a factor of a thousand.

As the final data acquisition method an ADC of 20 MHz or 40 MSps specification is being developed to be read out by an industrial Beagle Bone Black (BBB), a type of microcomputer.

This contrasts with the Arduino which is a microcontroller. The difference between the two is that a microcomputer has a dedicated processor, graphics card, flash storage, RAM and OS just like a desktop computer would have. A microcomputer can also have microcontrollers as a subsystem, which the BBB has two of. This microcomputer is used as it can operate across the required temperature range and it can execute python scripts, which will be used to process the information it receives from the ADCs (Foundation, 2014). The BBB is also capable of ethernet communication and can run a Linux OS, which is desirable for connecting the BBB to the satellite bus for data telemetry. Telemetry is also made easier by having 4 GB of dedicated storage, allowing the BBB to store data until the satellite bus is no longer busy and is ready to accept data for telemetry.

An initial incarnation of the python script to be run by the BBB has been developed. This script was tested with an undersampled, 40 MSps, version of the pulse used in the previous section. The result, seen in Figure 2.14, shows that the script can use a peak and valley finding algorithm to successfully find the peak of the scintillation and Cherenkov radiation and the valley point of the scintillation radiation.

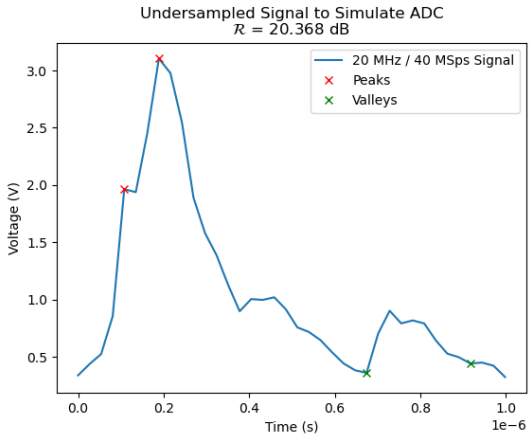

Figure 2.14: Undersampled scintillation and Cherenkov pulses, particularly undersampled to 40 MSps. The voltage of the signal is drastically increased as the integral voltage is conserved but the number of points is decreased. The value of Radiation Gain is then found by the python script. It is similar to the fully sampled version and within the range of the theory.

From these values $\mathscr{R}$ is calculated from the integral of the two pulses. In this case the integral of the Cherenkov radiation is one data point, only amplitude. The integral of the scintillation

pulse is then between the scintillation peak and the nearest valley. The peak and valley finding algorithm also screen for values of the peaks and valleys to screen out peaks and valleys that are not suitable. This screening is important to ensure that noise does not cause incorrect peaks and valleys to register. Even with this undersampling a similar value of $\mathscr{R}$ is found. This script will also be tuned against a larger volume of cosmic ray muon data before flight to ensure the reliability of this method and to document effects of undersampling.

Chapter 3

HiCalK

3.1 Objectives

High Altitude Calibration KUbeSat (HiCalK) will use a small ultra-broadband antenna and RF pulser to calibrate and synchronize the numerous upward looking RF experiments, particularly those in the UHF and VHF band (30-1000 MHz). These experiments are expected to see similar large scale RF events, such as solar flares, so cross calibrating and synchronizing is pivotal for large scale coincidence measurements. A map of some of the affected experiments can be seen in 3.1.

3.2 Bivaldi Antenna

For HiCalK the antenna must fit within KUbeSat-1. Due to other structures in the satellite the constraints are 8x8x8 cm^3. Such a small space would allow for a half wave dipole of 1.9 GHz, but this frequency is above the typical frequencies seen by ground experiments. A different approach, of using the perimeter of this volume, could allow for a have wave dipole of 469 MHz. While

this may be low enough, due to the Friis equation preferring the transmission of low frequency power it is best to obtain the lowest possible frequencies with the highest forward gain. For this reason, a Vivaldi antenna, a wideband antenna with a forward beam pattern, was chosen as the base design (Panzer, 2007). Prototypes made of wire and sheet metal were tried to middling success. Different geometries, such as having one Vivaldi, having two Vivaldis in a cross pattern, having two Vivaldis perpendicular, or having two Vivaldis anti-parallel, were tried. Eventually the perpendicular geometry was settled on with the antenna being printed on two circuit boards soldered together. After this multiple feed points were tested until it was discovered that the current feed point yielded the best performance at low frequencies. The antenna performance at this point was still poor below 200 MHz, likely due to difficulties for the two antenna halves to induce fields at wavelengths longer than their dimensions. To improve this the impedance matching was improved by including two 10 Ohm resistors in series to the two antenna halves. The process of using circuit elements like this, to improve antenna performance, is usually referred to as loading, with this being resistive loading. Despite antennas and circuit elements being old technologies, it is unknown when this technique began. There are two patents which cover this technique, one from the 1950s in Australia, whose source material is not public, and one from the 1970s in America (Willoughby, 1953) (Goodbody, 1972). The American patent was used to tune Navy antennas when the wavelengths of the antenna were larger than the physical size of the antenna. By using this loading technique not only can low frequency performance be improved but the propagation of the field on the antenna can be fine-tuned. A picture of the 7x7.5cm double Vivaldi, hence dubbed "Bivaldi", antenna can be seen in Figure 3.2.

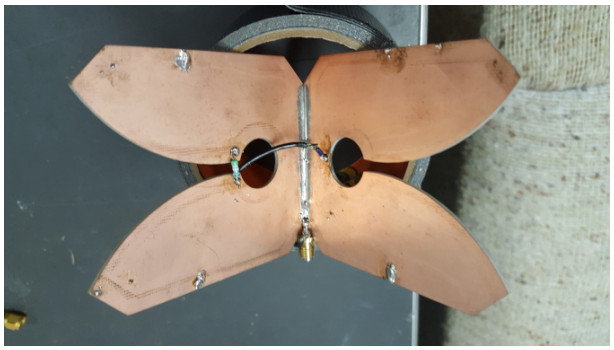

Figure 3.2: The Bivaldi antenna. The feed point is the SMA feed point at the bottom center. There is a cable that runs from the ground of the SMA feed point to the 10 Ohm resistor on the right side of the Bivaldi. The companion 10 Ohm resistor to this is on the left side. By using these resistors the field propagation on the antenna can be tuned.

To test the performance of the Bivaldi the standing wave ratio (SWR) was used many times. SWR is used as it essentially measures the ratio between a calibration impedance, typically 50 Ohms, and the antenna's impedance. This is complex impedance, so both resistance and reactance are matched and then the magnitude is used. For SWR a value of 1.0 is the minimum and characterizes perfect transmission. Performance decreases above 1.0 SWR with a SWR of 2.0 represents roughly 69% transmission and is often used as a benchmark for establishing the bandwidth of the antenna. The SWR of the Bivaldi can be seen in Figure 3.3.

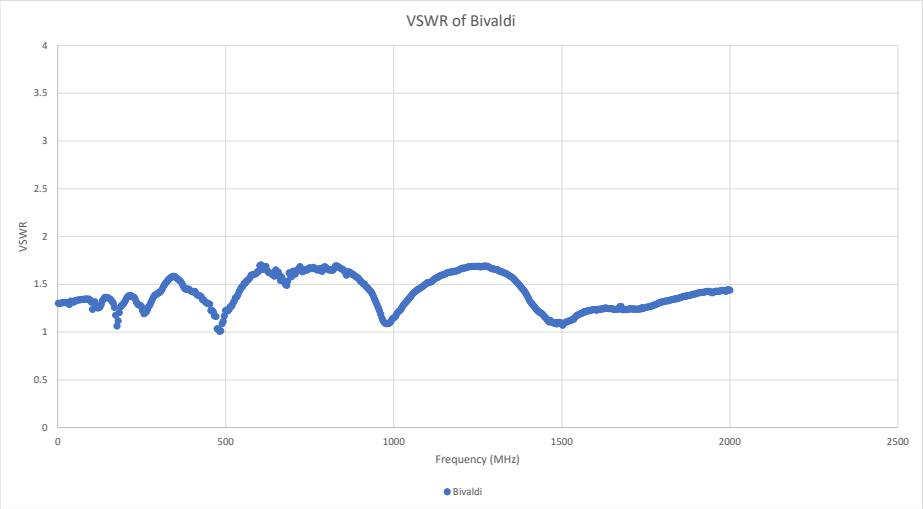

Figure 3.3: Bivaldi SWR as measured against a 50 Ohm calibration source. While it may look like this SWR gives the Bivaldi active bandwidth across the entire frequency probed here there are other effects that make this less true.

Using the 2 SWR cutoff this would indicate a bandwidth of 5 MHz, the lowest frequency, to 2 GHz, the highest frequency. This is likely not true for a few reasons. Firstly, this SWR comes from S11 measurements. In S11 measurements a network analyzer sends signals to an antenna and measures how they reflection. If there is no reflection, then it is assumed that the entire signal is transmitted. It does not factor in what direction the signal is transmitted. This is a considerable issue when the antenna must push all the power in one direction, as in this case. To better understand where the antenna power is going S21 measurements can be used. In S21 measurements one antenna sends a signal to a calibrated receiver antenna. This may be done at one angle or through a sweep of angles in a plane in order to measure the beam pattern. This was done in a sweep perpendicular to the faces of the Bivaldi. The resulting normalized beam patterns, in dB, at different frequencies and one pattern that has been then averaged over a $\frac{1}{freq.}$ signal, can

be seen in Figure 3.4.

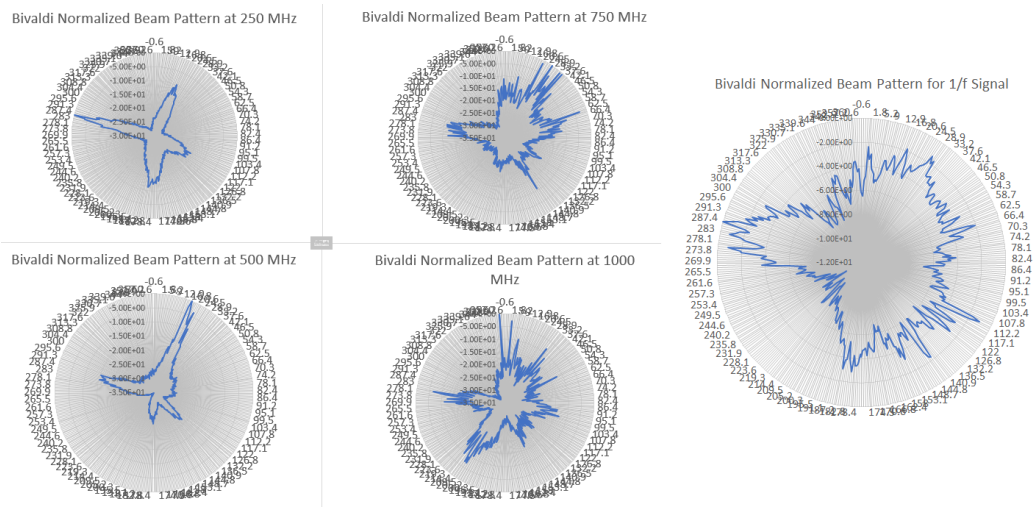

Figure 3.4: Bivaldi beam pattern measured in the plane perpendicular to both of the faces of the Bivaldi. The is one main lobe near 287 degrees that has a width of roughly 25 degrees.

As it can be seen the most powerful lobe, typically referred to as the main lobe, changes based off the frequency. At 250 MHz there is one main lobe near 287 degrees with two side lobes and one back lobe. By 500 MHz the side lobe at 15 degrees becomes the main lobe. By 750 MHz and 1000 MHz the main and side lobes have similar power. As such the high SWR bandwidth is effectively false as the antenna is changing where it is directing most of that power as the frequency changes. To address this, we instead characterize the performance using return loss (RL) which is expressed in dB and written as:

$$RL = 20 * \log_{10}(|\Gamma|) \tag{3.1}$$

Where the magnitude of the reflection coefficient, a.k.a. the S11 coefficient, is written as $|\Gamma|$. To determine bandwidth and acceptable performance we use a *RL* of 10 dB, which is close to the 2 SWR used prior. We can then use S21 measurements to adjust *RL* for the loss in directivity, i.e. how much dB the antenna loses in the main lobe because it pushes power into other directions. We derive the directive loss $\mathscr{D}$ as a function of frequency:

$$\mathscr{D}(f) = RL(f) - G(\theta_{main}, f) + G(\theta_{max}, f) \tag{3.2}$$

Where the gain, G, in the direction of the main lobe is given as $G(\theta_{main})$ and the gain in the direction of the maximum gain is given as $G(\theta_{max})$. Since these are all frequency dependent the max power lobe can be different from the main lobe, as was seen in Figure (22). Typically, this is not solved for as antenna, and their beam patterns, are usually investigated monochromatically. For wideband, i.e. large bandwidth, and directional antennas it is important to characterize this or else we will overestimate the performance. The results of using $\mathscr{D}$ alongside RL can be seen in Figure (23).

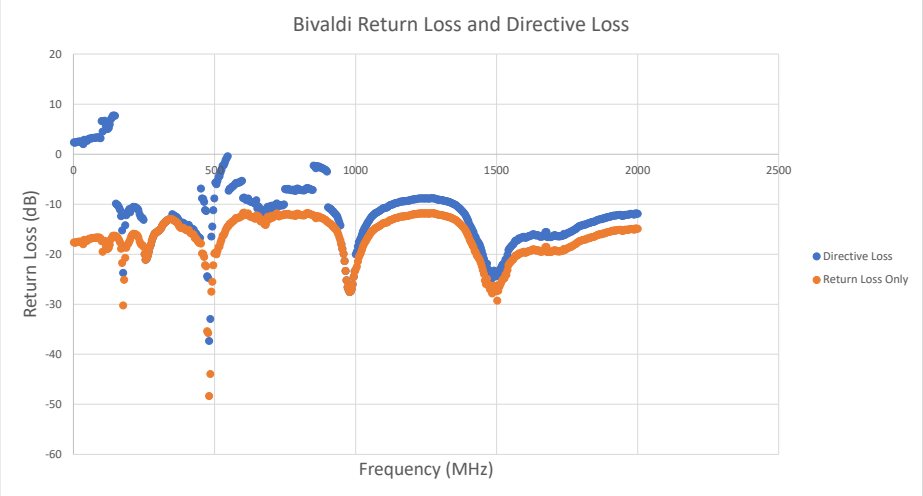

Figure 3.5: Bivaldi return loss and directive loss, $\mathscr{D}$, using S11 and S21 measured in the plane perpendicular to both of the faces of the Bivaldi. With this correction the anomalously high performance below 150 MHz becomes acceptingly poor.

With this correction the performance of the antenna adjusts and is poorer but closer to reality. The most noticeable change is that performance below 150 MHz has drastically been loss due to

the power of the main lobe being gone at lower frequencies. These lower frequencies see a mix of mostly isotropic radiation and wide lobes in directions different to the main lobe. With these corrections the antenna bandwidths up to 1 GHz are now 160-490 MHz, 630-750 MHz, and 900-1000 MHz. Since the signals being transmitted by the antenna are pulses it is also important that the antenna have a flat phase space. If an antenna crosses the entire phase space, often $-\frac{\pi}{2}$ to $+\frac{\pi}{2}$ is used, then the pulse performance is poor. This change in performance is due to antenna dispersion as wide band pulse signals can have some of the frequencies in the pulse deconstructively interfere. An example of a directive and wide band antenna type that has significant dispersion is a log periodic dipole antenna (LPDA). As such the LPDA antenna architecture was not pursued. The phase space for the Bivaldi can be seen in Figure 3.6.

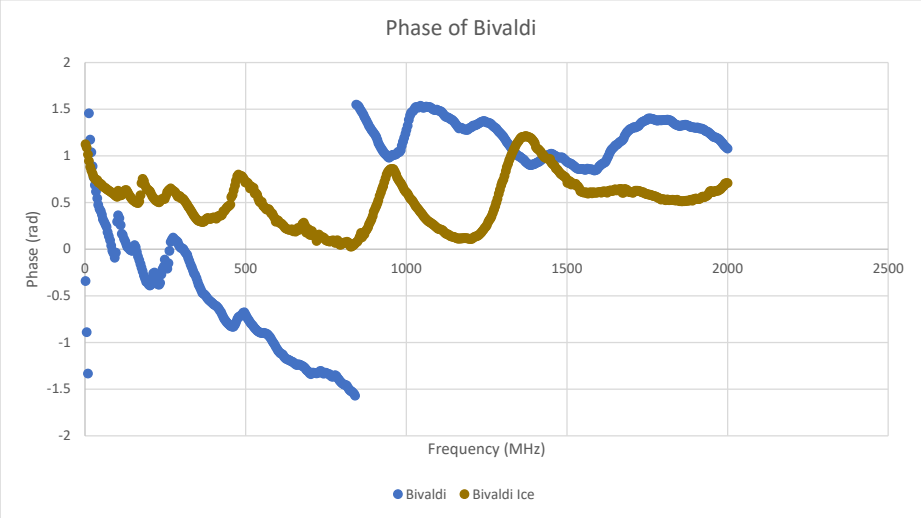

Figure 3.6: The phase space of the Bivaldi antenna is presented. This was measured against a 50 Ohm calibration source and then later recalculated as if the calibration source was replaced with one matching the impedance of ice. As such the phase space in 50 Ohms and in ice can be seen.

The phase space for air and ice was calculated using data from the S11 measurement. This

can be done for ice by converting the S11 measurement to complex impedance. Particularly this will be an impedance ratio of the calibration impedance used and the measured impedance. By multiplying out the calibration impedance, here 50 Ohms, and then dividing by the ice impedance the phase for ice can be calculated from the phase angle of the complex impedance. There is one crossing in phase space of air that can be seen, indicating minimal pulse dispersion. In the case of ice the antenna is mostly in phase, meaning that any transmitted pulse would mostly constructively interfere and maximize amplitude.

3.2.1 Pulse At Ground

Repeating the steps taken in section (1.1) we can derive what a pulse at ground from the Bivaldi at an altitude of 450 km would look like. First measurements of the transmission from Bivaldi to an ANITA horn were taken at 10 meters using a piezoelectric pulser. From this the Friis loss can be applied for the remaining 450 km. The resulting received power spectra can be seen in Figure 3.7.

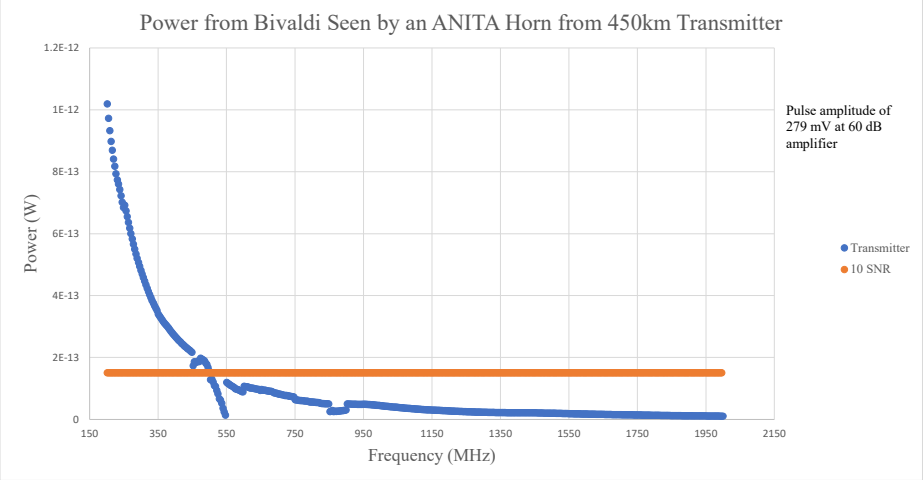

Figure 3.7: Power spectra as seen by an ANITA horn at ground from a Bivaldi transmitting from an altitude of 450 km. This was done by extrapolating out lab data to 450 km using Friis equation. Integrating this voltage, and factoring in the phase of each respective antenna, yields the pulse amplitude of 279 mV after applying 60 dB of gain from a 60 dB amplifier.

The noise floor is calculated using the Johnson-Nyquist noise for each bin bandwidth; the measurements used for this calculation were conducted with an oscilloscope with a bin bandwidth of 3.6 MHz at the setting used. Power below 450 MHz is above the noise floor and could be measurable. Integrating from a 200 MHz minimum frequency to the 450 MHz maximum frequency and adding 60 dB of gain from an amplifier gives a pulse amplitude of 279 mV. The power received would be equivalent to 21.6 SNR, meaning that this antenna should trigger the ground stations at full efficiency. Beam width was also determined to be roughly 25 degrees and so this affects the pulse rate, as it did in section (1.1). With said beam width the ground coverage would be 190 km with a minimum pulse rate of once per 83.4 seconds. This process can be repeated for different receiver antennas if lab transmission measurements are made. This is currently being planned for the KUbeSat-1 University of Kansas Lawrence campus ground station, but the ground station is

currently being constructed.

3.3 Pulser Background

To generate the radio pulses the HiCalK payload will broadcast there are a few pulsers that have been previously used. Here we will overview them and their development for HiCalK.

3.3.1 IDL Pulser

Developed by the University of Kansas Instrument Design Lab, the IDL pulser uses a series of avalanche diodes to generate a quick and high voltage discharge. This discharge is entirely internal, and no spark is generated. This discharge is done after a signal from a trigger source is sent. This is normally done by a microcontroller that is attached to the IDL pulser. By doing so the IDL pulser can be precisely controlled. Both qualities, no spark and precise timing, make the IDL desirable as a pulser. These advantages come at costs, particularly due to the avalanche diode performance. When these diodes avalanche the power spectrum is lower frequency, below 100 MHz, than other pulsers and the power peaks at the characteristic frequency of the diodes. This lower frequency bias is harder for small antenna, which usually broadcast higher frequency signals, to broadcast power. The overall power output of the IDL pulser is also the lowest of the pulsers presented here. Particularly it is too low power to have detectable signals reach the surface of Earth. For these reasons the IDL pulser was not further explored for HiCalK.

3.3.2 HVSP

Originally developed as a part of the SPICE experiment to characterize ice in Antarctica, the high voltage across a spark gap pulser or HVSP generates a radio pulse by generating a plasma discharge across two terminals (Allison et al., 2020). One terminal is brought to a high potential by a voltage multiplier that is powered by an oscillating circuit. As this terminal reaches higher and higher voltages one must consider Paschen's Law wherein the breakdown of air may occur and generate

a spark across the terminals. For half a centimeter this amounts to roughly 10 kV. This discharge also has an radio frequency (RF) component as the energies of discharged charges follows a $\frac{1}{freq.}$ distribution (PIM, 1948). Since Paschen's Law is dependent on the distance between the terminals and the gas, and its pressure, being discharged through the HVSP can be modified by changing either of those three parameters. The timing and power of the radio pulses is also heavily dependent on the power supply of the circuit and the distance of the terminals. To use HVSP in a space-borne payload would require either vacuum discharge, which is possible but dangerous to the surrounding spacecraft, or a pressure vessel for the terminals. The latter was pursued wherein tests were conducted to see how long HVSP could run when put inside a pressure vessel filled with Argon at 1 atm. of pressure. The plot of this test, with the ambient temperature also plotted, can be seen in Figure 3.8.

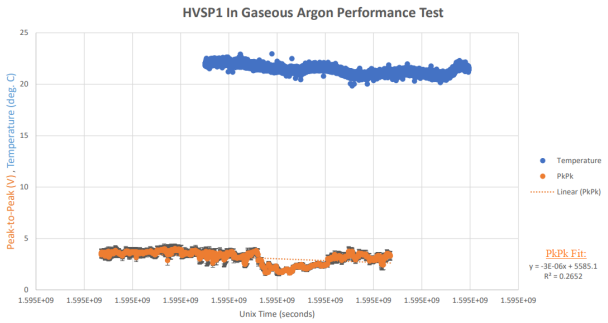

Figure 3.8: Result of running HVSP in a pressure vessel filled with Argon at 1 atm. of pressure. The offset in times for the temperature and peak-to-peak values is due to the temperature sensor being started late and then the pulser dyeing before the temperature sensor was stopped.

The peak-to-peak voltage of the RF pulse is plotted in orange with the ambient temperature plotted in blue. This test was conducted over five days. The trend across five days indicates a global decrease in the peak-to-peak with lots of variance over smaller time scales, particularly over the course of hours. After two days HVSP saw a large drop in performance but eventually recovered. On the fifth day the pulser had a sudden loss of performance that it did not recover from. The pulser did not recover until it was deconstructed and then reconstructed. No new parts were added in the reconstruction. It is not understood why this performance is so chaotic or why it failed after five days. One possible explanation is that the repeated discharge into the Argon

managed to charge parts of the circuit elements of HVSP until it could not operate normally. This explains the longer-term behavior but does not explain the large variance over shorter periods of time. Considering the short performance and the requirement of a pressure vessel filled with gas the HVSP was not further developed for HiCalK.

3.3.3 Piezoelectric

A piezoelectric pulser was used in previous HiCal missions, notably HiCal-2 (Prohira et al., 2019). For HiCal-2 the piezoelectric pulser consisted of a grill sparker that was activated by a motor. The leads of the sparker were fed into a bicone antenna. The spacing between the halves of the bicone antenna was then treated as a parameter for tuning. These antenna halves effectively act as discharging terminals, so the terminal separation relationship of Paschen's Law holds. This is then further complicated by the change in antenna performance that will occur as the antenna halves are moved. Therefore, the optimization of the performance for the HiCal-2 setup was done experimentally by varying the distance of the halves until an optimal distance was found. In recent developments tests with the piezoelectric pulser were conducted with discharging in vacuum and discharging through a wire. In both cases no significant change in performance was measured. It was also confirmed, using HVSP1, that an air discharge pulser dies in vacuum while the piezoelectric pulser does not. Instead the piezoelectric pulser switches over to vacuum arcing and then, at low enough pressure, to no visible spark while retaining its RF pulse generation. The operation of piezoelectric sparkers in vacuum is also seen in condensed matter experiments and has uses in rocket ignition both on Earth and in space (Wollen & Gruszczynski, 2011) (Shchagin et al., 2018). A comparison between HVSP1, the first HVSP made, and a piezoelectric pulser both running in a sealed environment can be seen in Figure 3.9.

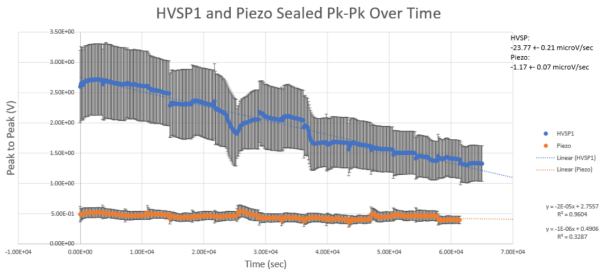

Figure 3.9: A comparison of the peak-to-peak of both the HVSP1 and piezoelectric pulsers. Both pulsers see degradation over time but the degradation of HVSP1 is greater than its standard deviations while the piezoelectric degradation is smaller than its standard deviations.

For HVSP1 significant degradation is seen. The piezoelectric pulser sees no statistically significant degradation which supports the previous vacuum and wire discharge findings that the piezoelectric discharge can generate RF signal without an atmosphere. At this point the piezoelectric pulser was chosen for further development and a piezoelectric sparker with a higher spring constant was chosen. The higher spring constant piezoelectric sparker can generate discharge that is 2-3 cm in length, longer than the original. The reason for this is that these piezoelectric sparkers use internal springs to launch internal hammers against ceramic piezoelectric cylinders which then use the piezoelectric effect to convert the mechanical stress to electricity. Using Paschen's Law with the longer distance of 2-3 cm gives a potential of 50-100 kV, making it the most powerful pulser presented here. Further development was complicated by the fact that the non-atmospheric discharge outcome was not expected for the piezoelectric pulser. High frequency and non-resonant discharge of piezoelectric are expected but not in the way seen here. To pivot towards model building it was found that the piezoelectric being used was the piezoelectric ceramic Sodium Bismuth Titanate (NBT). Following these a model for this discharge was derived.

3.3.4 Piezoelectric Modelling

3.3.4.1 Ferroelectric Pulse

Since piezoelectrics require internal permanent dipoles and an internal hysteresis relationship between the electric field and polarization field all piezoelectrics are also ferroelectric. To explain the

RF pulse generated by the piezoelectric one can investigate already existing uses for ferroelectrics along this line. Particularly explosive or high-pressure activation of ferroelectrics have been used in directed energy RF weapons where Mega-Watt pulses are used (Altgilbers, 2011). Checking the validity of this one needs to calculate the potential stored in each NBT crystal, particularly between the dipoles of each individual atom:

$$V_{dip.} \approx \frac{NQed}{4\pi\varepsilon_r\varepsilon_0 r^2} \tag{3.3}$$

Here we treat Q as the number of valence charges. Solved for N crystals with an average separation distance, d. Separation between atoms will be on the order of 2.5 Angstroms for NBT crystals (Aksel, 2012). At 10 centimeters from the piezoelectric and with 1 gram of NBT the potential is then 1.6 kV. This is higher than the 0.8 kV seen in the lab, but this can be explained as not activating or aligning all the dipoles in the material with the given activation. With this interpretation the more stress the piezoelectric experiences the more of these dipoles would align. After the dipoles are aligned by the mechanical stress, they relax towards zero potential but are unable to do so perfectly as they exist as forced damped oscillators. As such there is expected chaos where there should be multiple oscillations, or pulses, of various non-linearly related periods and amplitudes. This is observed in lab and was also observed during the HiCal-2 mission (Prohira et al., 2019). Using the mechanical coupling efficiency of NBT, the mechanical energy used, and the heat capacity results in a temperature increase of 0.00023 Kelvin. A low temperature is to be expected for an RF system.

Even with this order of magnitude calculation this does not explain why the oscillation occurs in the radio frequency domain. To explain this we must consider that, not only is chaos hard to characterize, but as this ferroelectric pulse is driven by piezoelectricity it should be reversible as piezoelectricity is reversible (Curie & Curie, 1881). Another kind of motion, Brownian motion, is also reversible and can be used to characterize chaos and, since it is possible to derive the spectral response of Brownian motion, we can use this to probe the frequency content of the potential generated.

3.3.4.2 Brownian Motion

We investigate models of piezoelectricity based in Brownian motion as both Brownian motion and piezoelectricity can be reversible (Pavliotis, 2014). One important feature of Brownian motion is that radiation comes from the deviations in the average motion, not the motion itself (Einstein, 1905). Brownian motion can be used to describe particle motion or used to describe bulk phenomenon that arise from Brownian motion, as in the case with Johnson-Nyquist noise. Regarding this Einstein originally worked on translational Brownian motion with the motion of water and pollen cells, in doing so derived that the average deviation in wavelength (Chodos & Ouellette, 2005):

$$\sigma_\lambda = \sqrt{2Dt} \tag{3.4}$$

Where D is the thermal diffusion coefficient and t is the time to equilibrium. The thermal diffusion coefficient for a medium can be derived:

$$D = \frac{k_T}{\rho c_p} \tag{3.5}$$

Where the thermal conductivity, k_T, is being divided by the product of the mass density ρ and heat capacity c_p. From this we can extend this relationship to the average deviation in frequency:

$$\sigma_f = \frac{c}{\sqrt{2\varepsilon_r Dt}} = \sqrt{\frac{c^2 \rho c_p}{2\varepsilon_r k_T t}} \tag{3.6}$$

Where the root of relative permittivity, ε_r, is used as the index of refraction of the medium. From this equation materials that are more conductive, lower heat capacity, lower density, will dissipate at lower frequencies. This can be applied to piezoelectric discharge where oscilloscope measurements show that piezoelectricity occurs over the time scale of 0.001 to 1 seconds. Using reference values for the piezoelectric being used, NBT, gives a value of 44.5 GHz for a relaxation of one second which is well above the values expected from measurements (Aksel, 2012). Instead

individual atoms within the NBT structure can be looked at. Consider the structure of NBT as presented in Figure 3.10.

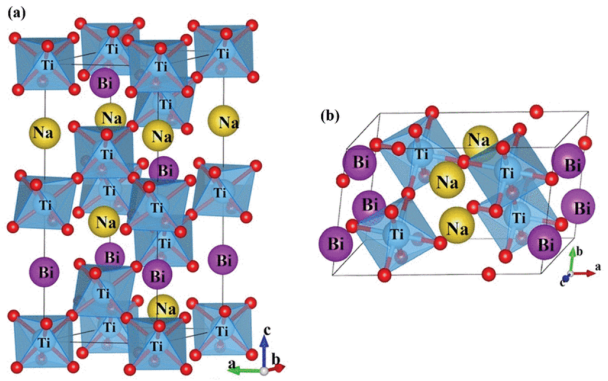

Figure 3.10: The crystal structure of NBT as presented in (Reichmann et al., 2015).

The structure reveals that the sodium and bismuth atoms fill the vacancies in the lattice, which make the average distance between these atoms and the oxygen atoms 2.75 Angstroms compared to the 1.98 Angstroms of the titanium and oxygen atoms (Reichmann et al., 2015). The bismuth and sodium atoms are quite different despite having similar roles. The electronegativity of bismuth is roughly four times sodium, it can have more bonds, it has a mass roughly nine times sodium and the ratio of bismuth's heat capacity to heat conductivity is roughly 12.0. Sodium on the other hand has a ratio of heat capacity to heat conductivity of 8.79, meaning that lower frequency Brownian motion would be expected of the Sodium atom. It is also known that certain preparations of NBT have high thermal conductance along the vacancies that the sodium atoms inhabit (Yang et al., 2020). Recalculating the frequency where the dominant part of the Brownian motion of NBT would be from the sodium atoms gives a frequency of 405 MHz for a relaxation of one second. This may seem odd, as a quantum particle should follow quantum descriptions, but it has been shown that certain forms of quantum Brownian motion recover classical Brownian motion (Attal et al., 2006). While this is closer it is still too high frequency to explain the entirety of the dissipated power. This effect may exist but there must also be another interaction.

We move to rotational Brownian motion, again following the work done by Einstein (Einstein, 1906). It is found that the average deviation in angle is:

$$\sigma_\theta = \sqrt{\frac{kTt}{4\pi\eta P^3}} = \sqrt{\frac{k_T t}{\rho c_p P^2}} \tag{3.7}$$

Where the viscosity of the media, η, and the size of the particle, P, is used. The viscosity is substituted for terms related to the heat conductivity and heat capacity as done before. Following this the average frequency deviation can be found from the time differential:

$$\sigma_f = \frac{1}{2\pi}\frac{\partial\sigma_\theta}{\partial t} = \frac{1}{4\pi}\sqrt{\frac{k_T}{\rho c_p P^2 t}} \tag{3.8}$$

Calculating this for the 9.5 Angstrom diameter of the NBT unit cell and a time of 1 second gives 18.2 kHz, which is near the lower limit of the piezoelectric effect and will be treated as the at rest time (Aksel, 2012). Repeating this for 1 nano-second, which is comparable to the finite width of the piezoelectric radio frequency pulse, gives 577 MHz. Both the lower end and upper end of frequencies overlap the audio and radio frequency bandwidths typically covered by piezoelectricity, which is promising. To test reversibility the time constant of Brownian motion can be used (Pathria & D., 2011). For the angular deviation this is then:

$$\tau = \frac{4\pi\eta P^3}{kT} = \frac{\rho c_p P^2}{k_T} \tag{3.9}$$

As there is no current measure of viscosity of NBT, the viscosity of a similar ceramic piezoelectric is used (Xu et al., 2015). This then gives a time constant of 0.79 seconds. From the reference, for times much smaller than τ, the process is reversible. Meaning that, for times much smaller than 0.79 seconds, e.g. 5 milliseconds, piezoelectricity should be reversible. Thus, with exception to the slowest parts of piezoelectricity, piezoelectricity should then be reversible, as measured by the Curies in 1881 (Curie & Curie, 1881). This is the expected case but, considering this was set out as conjecture, the dipole ferroelectric and rotational Brownian motion model of piezoelectricity needs to be further proven. This model is also currently blind to the stress imparted onto the piezoelectric so, while it has nicer theoretical features than current models, it is lacking in features key to predicting engineering solutions.

3.3.4.3 Stress Response

In order to determine ways to improve the piezoelectric instrumentation the stress response was tested. Firstly, the stress can be written as:

$$T = \frac{F}{A} = \frac{E}{xA} \tag{3.10}$$

Where the stress, T, is the quotient of F, the force, and A, the area, or similarly of the energy E and the product of the penetration depth, x, and area. The maximum penetration depth can be found from the product of the total length, L, the electric field and the piezoelectric charge constant d_{ij}:

$$x = L|\vec{E}|d_{ij} \tag{3.11}$$

There are indices on the piezoelectric charge constant because it is a tensor quantity and, for piezoelectric instrumentation, the index values used correspond to the method and direction of stress being used. For the setup here x is roughly 10 nanometers. The stress is expected to be linearly related to the voltage, linearized by the piezoelectric voltage constant g_{ij} (Xu, 2016). Similar use of indices apply to g_{ij} as d_{ij}. Thus, increasing the drop height and the activated area should both be linear with the output voltage. An experiment was conducted to test the linear relationship between voltage and mechanical stress. Two sections of NBT ceramic were created, one of a full width of 1.05 centimeters, and the second with a half-width cut to 0.51 centimeters. These segments were then wrapped in wire and the wire fed to an oscilloscope. Then a 0.091 kilogram mass was dropped onto these ceramics, repeatedly, from the same set of heights as measured by a meter stick. As this happened the RF pulse generated was read-out on an oscilloscope. The amplitude of the peak would then be recorded. To keep the penetration roughly constant the drop heights were similar as, if the piezoelectric electric field gets large enough the penetration depth will change per Equation 3.11. The surface of the ceramic struck was also kept the same between the strikes and the ceramic sections in order to keep d_{ij} term in Equation 3.11

constant. The results can be seen in in Figure 3.11, where the LINEST fit gave a slope value of $26.03 \pm 4.75 \frac{V}{J}$ for the half-width ceramic and $12.21 \pm 1.03 \frac{V}{J}$ for the full-width ceramic. From the ratio of these values one gets a value commensurate with two, 2.13 ± 0.40.

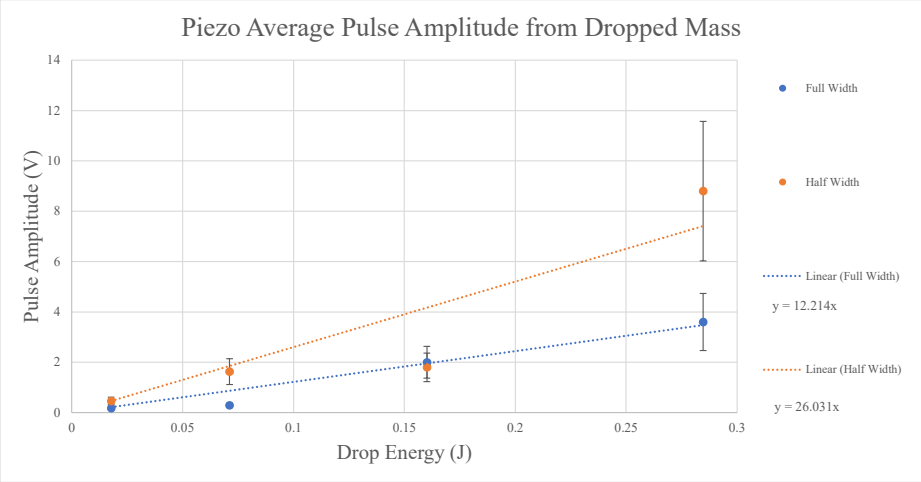

Figure 3.11: The piezo pulse amplitude was plotted against the gravitational energy of the dropped mass it was struck with. Linear relationships are seen for both the full and half width piezo ceramics.

Using the stress response measurements done here it can be seen that optimizing the mechanical stress, and the output voltage, is more effective when minimizing the area being mechanically struck. The simplicity and low cost of this experimental setup, assuming one has access to an oscilloscope, could make this experiment good for intermediate level physics labs for demonstrating mechanical stress and piezoelectricity.

Chapter 4

Conclusion

In chapter 1 the KUbeSat-1 mission and contextual space and aerospace physics were presented. The payloads and baselines for the HiCalK payload was presented and derived. Some of the engineering capabilities of the KUbeSat-1 satellite were given and back up claims that this craft can fly the HiCalK payload. In chapter 2 the PCRD payload was presented. Wherein development of a novel technique, using the radiation gain or $\mathscr{R}$ parameter, to increase the ability to discriminate particles within a small volume particle detector. The instrumentation and read-out techniques investigated were discussed with the current favor being for a custom ADC readout by a BBB. In chapter 3 the HiCalK payload and its development was presented. A new type of wideband radio antenna, the Bivaldi, inspired by maximizing the surface area of a Vivaldi antenna within the area of a CubeSat, was developed. It showed ultra-wide band performance, from 200-2000 MHz, and a main lobe beam-width of 25 degrees. Three RF pulser architectures were investigated with the most powerful, the piezoelectric pulser, being chosen. The piezoelectric pulser was found to pulser and operate in previously unexplained ways. As such a model and interpretation of these results was made. Particularly the piezoelectric response was modeled as a ferroelectric oscillator with rotational Brownian motion. The relationship of mechanical stress and energy were related to the output voltage. The expected piezoelectric relationship of voltage to input stress was recovered. The experimental setup used was fairly simple and cheap, possibly being accessible to students.

References

Aab, A., Abreu, P., & al. (2018). An indication of anisotropy in arrival directions of ultra-high-energy cosmic rays through comparison to the flux pattern of extragalactic gamma-ray sources. *The Astrophysical Journal*, 853(2), L29.

Adriani, O. et al. (2017). Ten years of PAMELA in space. *Riv. Nuovo Cim.*, 40(10), 473–522.

Aguilar, M. et al. (2013). First Result from the Alpha Magnetic Spectrometer on the International Space Station: Precision Measurement of the Positron Fraction in Primary Cosmic Rays of 0.5–350 GeV. *Phys. Rev. Lett.*, 110, 141102.

Aksel, E. (2012). *Structure and properties of sodium bismuth titanate ferroelectric ceramics*. PhD thesis.

Allison, P., Archambault, S., Beatty, J. J., Besson, D. Z., Chen, C. C., Chen, C. H., Chen, P., Christenson, A., Clark, B. A., Clay, W., Connolly, A., Cremonesi, L., Deaconu, C., Duvernois, M., Friedman, L., Gaior, R., Hanson, J., Hanson, K., Haugen, J., Hoffman, K. D., Hong, E., Hsu, S. Y., Hu, L., Huang, J. J., Huang, A. M. H., Hughes, K., Ishihara, A., Karle, A., Kelley, J. L., Khandelwal, R., Kim, M. C., Kravchenko, I., Kruse, J., Kurusu, K., Kuwabara, T., Latif, U. A., Laundrie, A., Li, C. J., Liu, T. C., Lu, M. Y., Madison, B., Mase, K., Meures, T., Nam, J., Nichols, R. J., Novikov, A., Nozdrina, A., Oberla, E., Pan, Y., Pfendner, C., Relich, M., Sandstrom, P., Seckel, D., Shiao, Y. S., Shultz, A., Smith, D., Song, M., Torres, J., Touart, J., Varner, G. S., Vieregg, A., Wang, M. Z., Wang, S. H., Wissel, S., Yoshida, S., & Young, R. (2020). Long-baseline horizontal radio-frequency transmission through polar ice.

Altgilbers, L. L., Ed. (2011). *Explosive pulsed power*. London: ICP, Imperial College Press. OCLC: 837749819.

ATMEL (2013). 8-bit Microcontroller with 4/8/16/32K Bytes In-System Programmable Flash p. 246. https://www.sparkfun.com/datasheets/Components/SMD/ATMega328.pdf. Online: accessed Summer 2020.

Attal, S., Joye, A., & Pillet, C.-A., Eds. (2006). *Open quantum systems*. Number 1880-1882 in Lecture notes in mathematics. Berlin ; New York: Springer. OCLC: ocm70132630.

Brace, L. H. & Spencer, N. W. (1963). Ionosphere electron temperature measurements and their implications. *Journal of Geophysical Research*, 68(19, p. 5397).

Chodos, A. & Ouellette, J. (2005). This month in physics history.

Curie, J. & Curie, P. (1881). Comptes rendus hebdomadaires des séances de l'Académie des sciences / publiés... par MM. les secrétaires perpétuels.

DIGILENT (2016). Basys 3™ FPGA Board Reference Manual. https://reference.digilentinc.com/_media/basys3:basys3_rm.pdf. Online: accessed Summer 2020.

Einstein, A. (1905). Uber die von der molekularkinetischen theorie der warme geforderte bewegung von in ruhenden flussigkeiten suspendierten teilchen. *Annalen der Physik*, 322(8), 549–560.

Einstein, A. (1906). Zur Theorie der Brownschen Bewegung. *Annalen der Physik*, 324(2), 371–381.

Foundation, B. (2014). USER MANUAL element14 BeagleBone Black *System Reference Manual*. https://cdn.sparkfun.com/datasheets/Dev/Beagle/e14%20BBB_SRM_rev%200.9.pdf. Online: accessed Summer 2020.

Frank, I. & Tamm, I. (1937). Coherent visible radiation of fast electrons passing through matter. *Compt. Rend. Acad. Sci. URSS*, 14(3), 109–114.

Friedel, R. A., Orchin, M., & Rosenbaum, E. J. (1952). Ultraviolet spectra of aromatic compounds. *Applied Spectroscopy*, 6(2), 38–38.

Gallardo-Lacourt, B., Liang, J., & Nishimura, Y. (2018). On the origin of steve: Particle precipitation or ionospheric skyglow? *Geophysical Research Letters*, 45.

Goodbody, R. (1972). Resistive loading technique for antennas.

Gorham, P., Allison, P., Banerjee, O., Beatty, J., Belov, K., Besson, D., Binns, W., Bugaev, V., Cao, P., Chen, C., Chen, P., Clem, J., Connolly, A., Dailey, B., Dasgupta, P., Deaconu, C., Cremonesi, L., Dowkontt, P., Fox, B., Gordon, J., Hill, B., Hupe, R., Israel, M., Jain, P., Kowalski, J., Lam, J., Learned, J., Liewer, K., Liu, T. C., Matsuno, S., Miki, C., Mottram, M., Mulrey, K., Nam, J., Nichol, R., Novikov, A., Oberla, E., Prohira, S., Rauch, B., Romero-Wolf, A., Rotter, B., Ratzlaff, K., Russell, J., Saltzberg, D., Seckel, D., Schoorlemmer, H., Stafford, S., Stockham, J., Stockham, M., Strutt, B., Tatem, K., Varner, G., Vieregg, A., Wissel, S., Wu, F., & Young, R. (2017). Antarctic surface reflectivity measurements from the anita-3 and hical-1 experiments.

Group, P. D., Beatty, J. J., & et al. (2019). Cosmic rays.

Hamm, K. R. & al. (2019). 2019, NASA Engineering and Safety Center NESC Technical Update. `https://www.nasa.gov/sites/default/files/atoms/files/nesc_techupdate_2019_one-page.pdf`.

Kamide, Y. & Chian, A. (2007). *Handbook of the Solar-Terrestrial Environment*. Berlin: Springer.

KETEK (2019). Product Data Sheet SiPM – Silicon Photomultiplier PM3315-WB-B0, Rev. 07/2019. `https://www.ketek.net/wp-content/uploads/2018/12/KETEK-PM3315-WB-B0-Datasheet.pdf`. Online: accessed Summer 2020.

Kulu, E. (2020). Nanosatellite & CubeSat Database.

Lubis, B., Ramachandra, N., Madison, B., & Besson, D. (2017). KUbeSat Primary Cosmic Ray Detector (KUbeSat PCRD). *SPS National*, 2017 Chapter Research Award.

Mahoney, E. (2014). CubeSat Launch Initiative: 50 CubeSats from 50 States in 5 Years. `https://www.nasa.gov/content/`

cubesat-launch-initiative-50-cubesats-from-50-states-in-5-years. Online: accessed Summer 2020.

Mewaldt, R. A. e. a. (2001). Long-term fluences of energetic particles in the heliosphere.

NIST (1998). ESTAR: Stopping Powers and Ranges for Electrons. https://physics.nist.gov/PhysRefData/Star/Text/ESTAR.html.

NIST, Berger, M. J., & al. (1998). Stopping-Power & Range Tables for Electrons, Protons, and Helium Ions. https://physics.nist.gov/PhysRefData/Star/Text/PSTAR.html.

Panzer, B. (2007). *Development of an Electrically Small Vivaldi Antenna: The CReSIS Aerial Vivaldi (CAV-A)*. Thesis, University of Kansas.

Pathria, R. K. & D., B. P. (2011). *Statistical mechanics*. Oxford; Boston: Butterworth-Heinemann, 3 edition. OCLC: 182559775.

Pavliotis, G. A. (2014). *Stochastic Processes and Applications: Diffusion Processes, the Fokker-Planck and Langevin Equations*. Texts in Applied Mathematics. New York: Springer-Verlag.

Pazianotto, M., Cortés-Giraldo, M., Federico, C., Gonçales, O., Hubert, G., Quesada, J., & Carlson, B. (2018). Analysis of the angular distribution of cosmic-ray-induced particles in the atmosphere based on monte carlo simulations including the influence of the earth's magnetic field. *Astroparticle Physics*, 97, 106 – 117.

PDG (1999). PARTICLE DETECTORS , Particle Data Group p. 24. https://pdg.lbl.gov/2000/pardetrpp.pdf. Online: accessed Summer 2020.

PDG, Groom, D. E., & Klein, S. R. (2019). Passage of Particles Through Matter. https://pdg.lbl.gov/2019/reviews/rpp2018-rev-passage-particles-matter.pdf. Online: accessed Summer 2020.

Peterson, L. (2019). KU engineering students work on KUbeSat satellite for 2020 launch. https://www.kansan.com/news/

ku-engineering-students-work-on-kubesat-satellite-for-launch/article_43dec85a-e607-11e9-ad7a-7331032fa9d2.html. Online: accessed Summer 2020.

PIM, J. A. (1948). Electrical breakdown strength of air at ultra high-frequencies. *Nature*, 161(4096), 683–684.

Prinsloo, A. & et al. (2020). KUbeSat Launch. https://www.launchku.org/project/20260. Online: accessed Summer 2020.

Prohira, S., Novikov, A., Besson, D., Ratzlaff, K., Stockham, J., Stockham, M., Clem, J., Young, R., Gorham, P., Allison, P., & et al. (2019). Hical 2: An instrument designed for calibration of the anita experiment and for antarctic surface reflectivity measurements. *Nuclear Instruments and Methods in Physics Research Section A: Accelerators, Spectrometers, Detectors and Associated Equipment*, 918, 60–66.

Reichmann, K., Feteira, A., & Li, M. (2015). Bismuth sodium titanate based materials for piezoelectric actuators. *Materials*, 8, 8467–8495.

Rombeck, T. (2005). CubeSat could put KU in orbit. https://www2.ljworld.com/news/2005/mar/05/cubesat_could_put/. Online: accessed Summer 2020.

Sawyer, D. & Vette, J. (1976). AP-8 trapped proton environment for solar maximum and solar minimum. https://ccmc.gsfc.nasa.gov/modelweb/magnetos/AP-8-min-max-76-6.pdf. Online: accessed Summer 2020.

Shchagin, A. V., Miroshnik, V. S., Volkov, V. I., Kubankin, A. S., & Ivashchuk, O. O. (2018). Ceramic Piezoelectric Transformer in Vacuum for Acceleration of Electrons and Production of X-Rays. *Materials*, 11(7).

T. Kaptanoglu and M. Luo and J. Klein (2019). Cherenkov and scintillation light separation using wavelength in LAB based liquid scintillator. *Journal of Instrumentation*, 14(05), T05001–T05001.

Tascione, T. F. (2004). *Introduction to the Space Environment*. Krieger Publishing Company, 2 edition.

Tyvak (2020). Tyvak Nano Satellites, A Terran Orbital Corporation. `https://www.tyvak.com/contact/`. Online: accessed Summer 2020.

Vette, J. (1991). The AE-8 trapped electron model environment. Online: accessed Summer 2020.

von Krosigk, B. and Neumann, L. and Nolte, R. and et al. (2013). Measurement of the proton light response of various LAB based scintillators and its implication for supernova neutrino detection via neutrino–proton scattering. *Eur. Phys. J. C 73 2390*.

Willoughby, E. O. (1953). An improved wide band aerial.

Wilson, G. & al. (2016). Small Satellite Materials and Components Space Survivability Assessment with Space Environments Effects Test Facility.

Wollen, M. & Gruszczynski, M. (2011). Propellant Flow Actuated Piezoelectric Rocket Engine Igniter | SBIR.gov.

XILINX (2018). Vivado Design Suite User Guide *High-Level Synthesis*. `https://www.xilinx.com/support/documentation/sw_manuals/xilinx2017_4/ug902-vivado-high-level-synthesis.pdf`. Online: accessed Summer 2020.

Xu, J., Yang, M., ke, G., Qu, Y., Zhang, X., Ma, N., Wang, Y., & Yang, J. (2015). Enhanced piezoelectric properties of pzt ceramics prepared by direct coagulation casting via high valence counter ions (dcc-hvci). *Ceramics International*, 42.

Xu, T. B. (2016). 7 - Energy harvesting using piezoelectric materials in aerospace structures. In F.-G. Yuan (Ed.), *Structural Health Monitoring (SHM) in Aerospace Structures* (pp. 175–212). Woodhead Publishing.

Yang, F., West, A. R., & Sinclair, D. C. (2020). Non-ohmic conduction in sodium bismuth titanate: the influence of oxide-ion conduction. *Physical Chemistry Chemical Physics*, 22(36), 20941–20950.